Available online at www.sciencedirect.com
ScienceDirect
Comput. Methods Appl. Mech. Engrg. 197 (2008) 3057–3079
Computer methods in applied mechanics and engineering
www.elsevier.com/locate/cma

Treatment of acoustic fluid–structure interaction by localized Lagrange multipliers: Formulation

Michael R. Ross [a,*], Carlos A. Felippa [b], K.C. Park [b], Michael A. Sprague [c]

[a] *Analytical Structural Dynamics Department, Sandia National Laboratories, P. O. Box 5800, MS 0346, Albuquerque, NM 87185-0346, USA*
[b] *Department of Aerospace Engineering Sciences and Center for Aerospace Structures, University of Colorado, Campus Box 429, Boulder, CO 80309, USA*
[c] *School of Natural Sciences, University of California, P.O. Box 2039, Merced, CA 95344, USA*

Received 22 June 2007; accepted 8 February 2008
Available online 26 February 2008

Abstract

A new concept is presented for modeling the dynamic interaction between an acoustic fluid and an elastic structure. The coupling of this multiphysics system is done by inserting a kinematic interface frame between the fluid and the structure, and using node-collocated Lagrange multipliers to connect the frame to each subsystem. The time-domain response analysis is performed by a partitioned analysis procedure. The main advantages of this localized Lagrange multiplier (LLM) primal-dual coupling method are: complete localization of the structure and fluid subsystems, elimination of the conventional predictor in the partitioned time integration method, and the ability to accommodate non-matching meshes. The standard Newmark time integrator is used on both the fluid and structure models. It is shown that if the integrator is A-stable and second-order accurate for a monolithic treatment, it retains those properties for both Mortar and LLM partitioned solution procedures. Infinite and finite piston problems are used to explain and verify the methodology. A sequel paper under preparation presents and discusses a set of benchmark and application examples that involve the response of existing dams to seismic excitation.

Keywords: Coupled systems; Fluid–structure interaction; Earthquake dynamics; Partitioned analysis; Non-matching meshes; Lagrange multipliers

1. Introduction

The dynamic interaction between a fluid and a structure is a significant concern in many engineering problems. These include systems as diverse as aircraft, rockets, turbines, marine structures (fixed, floating and submerged), airbags, parachutes, storage tanks, dams, biomechanical systems, inkjet printers and suspension bridges. The interaction may change the dynamic characteristics of the structure and consequently its response to transient, periodic and stochastic excitation. The model-based simulation of this class of coupled multiphysics systems presents three technical challenges.

The first is *discretization heterogeneity*. Effective space and time discretization methods for the two interacting components are not necessarily the same. This dilemma is particularly pressing when one would like to use available but separate computer codes for the fluid and the structure treated as individual entities, and use them to solve the coupled problem.

The second is effective treatment of the interaction when the discrete structure and fluid meshes *do not match* over the interface. Non-matching spatial meshes may occur for various reasons: a component may require a finer mesh for accurate results; teams using different programs construct or generate the meshes separately; or the discretization of one or both components is determined *a priori* for other reasons, for example incremental simulation of the structure construction process. If different time-stepping schemes are used (for example, implicit in the structure and explicit in the fluid), solutions may not match in time either.

The third is *forestalling performance degradation* in simulations. Even if the separate discrete models are satisfactory

* Corresponding author.
E-mail address: mross11a@gmail.com (M.R. Ross).

0045-7825/$ - see front matter © 2008 Elsevier B.V. All rights reserved.
doi:10.1016/j.cma.2008.02.017

as regards to stability and accuracy, the introduction of interaction may have damaging effects on the coupled response. Furthermore, if the coupled components have widely different physical characteristics (stiffness, mass density, etc.), the coupled system may be scale-mismatched by orders of magnitude. A poorly scaled discrete model may produce unacceptable errors, particularly under long-term periodic or cyclic loading.

This paper presents the development of a primal-dual coupling method for treating the interaction of an acoustic fluid with a flexible structure, with emphasis on handling spatially *non-matching* meshes. This is called the localized Lagrange multiplier (LLM) method. A *frame* is introduced as "mediator" device between the fluid and the structure over the interaction surface. The frame is discretized in terms of kinematic (primal) variables. A Lagrange multiplier field is introduced between the frame and the structure, and another one between the frame and the fluid. The function of the multiplier pair is weak enforcement of kinematic continuity. This configuration completely decouples the structure and fluid models because each "talks" to the frame through node-collocated multipliers, and not directly to each other. Decoupling simplifies the construction of separate discretizations using different mesh generation programs, the use of customized solution methods (in particular methods available in existing codes) and the implementation of parallel processing.

To advance the solution in time, the LLM interface treatment is combined with a partitioned solution procedure. The time-stepping computations are organized in a way that *eliminates the conventional local prediction step* characteristic of staggered solution procedures. The next-step interface variables, Lagrange multipliers and frame accelerations, are obtained by solving an algebraic system of equations. Interface forces are fed to advance the fluid and structure state. The implicit interface treatment forestalls the well known stability degradation caused by conventional prediction schemes while retaining the desirable localization features of partitioned analysis procedures. Numerical computations indicate that if A-stable integration schemes, such as the trapezoidal rule, are chosen for the fluid and structure, the coupled system retains A-stability, and thus the time step is controlled by accuracy only. This result is proven in Appendix A for the Newark time integrator under certain restrictions. The use of implicit–explicit integration schemes and subcycling remains to be investigated.

2. Driver application problem

The driver application for testing this coupling method on fluid–structure interaction (FSI) problems is a concrete dam on flexible soil. The dam is subject to seismic excitation through base ground motion. Fig. 1 depicts a cross section of a realistic problem of this nature, in which abutments are not shown. (This is not an actual dam configuration, but a composite pieced together from several construction and site scenarios. Calculations reported in a sequel paper [46] were carried out on 2D and 3D models of existing dams.)

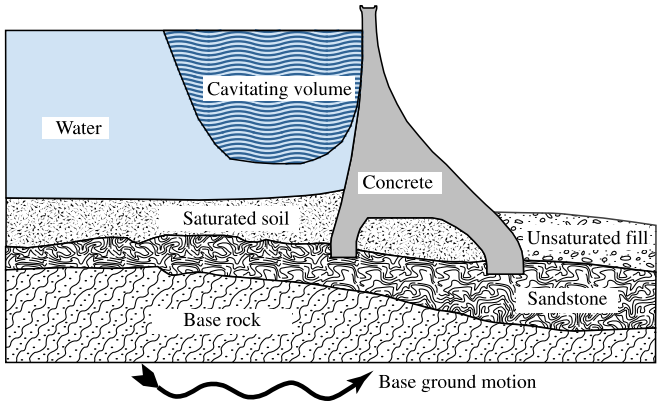

Fig. 1. Concrete dam on a flexible foundation subjected to seismic excitation.

Model-based simulations involve the interaction of the structure, near-field soil and stored water. For seismic response analysis, the water may be modeled as an acoustic fluid since no significant flow develops during the time span of interest. Two ancillary phenomena may occur. First, water near the vibrating dam may be subject to inertial cavitation [10]. This is a highly nonlinear phenomenon caused by a dynamic pressure drop that overcomes the hydrostatic pressure. Over the cavitating volume the macroscopic fluid elastic modulus drops to near zero while the mass density remains sensibly constant. Repressurization produces potentially damaging closure shocks. Second, the reservoir free surface may develop sloshing (gravity wave) oscillations [16,29]. Although sloshing is included in our fluid model, it normally has no significant FSI effect given its localized character and low associated vibration frequencies.

Following standard techniques of partitioned analysis [15,17,34,35] the problem can be divided into three partitions: structure, soil and fluid, as illustrated in Fig. 2a. The structure and soil are treated with standard finite element discretization procedures of structural mechanics, which lead to a system of semidiscrete equations of motion in the nodal displacements. For the acoustic fluid, however, the displacement potential (a scalar field) is the preferred primary variable on account of advantages discussed later. Linking displacement potentials to actual displacements is not a simple matter, since it requires consideration of fluid element patches. For this reason the fluid model is initially formulated in terms of displacements.

In previous FSI work that focused on underwater shock on submarines [15] and shallow depth attacks on surface ships [47], matching was done by transforming fluid pressures to structural node forces and structural velocities to fluid node forces. These are relayed from fluid to structure and vice-versa, at each time step of a staggered solution procedure. Such procedures necessarily incorporate predictors and have to be carefully designed to avoid stability degrada-

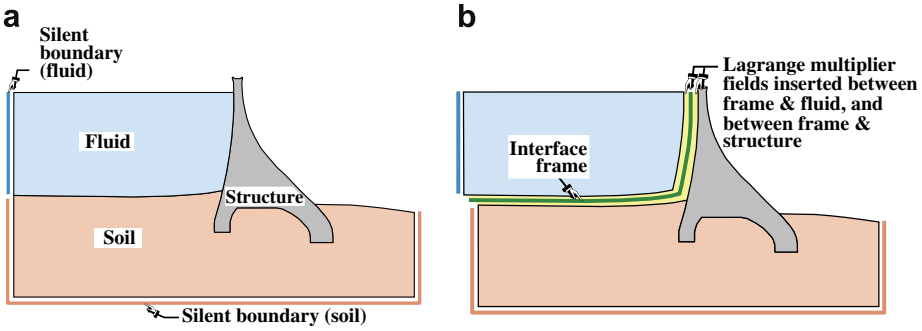

Fig. 2. Dam problem as coupled system: (a) physical partition, (b) LLM interface treatment.

tion. For example in the original staggered method developed in [34] for underwater shock, a modification of the fluid equations was required to attain unconditional stability.

Here the fluid–structure interface is treated by the LLM method by inserting a kinematic frame between those subsystems, as illustrated in Fig. 2b. Two Lagrange multiplier fields take care of the communication between the frame and adjacent boundaries. Multipliers are discretized with delta functions collocated at interface nodes. This arrangement simplifies handling non-matching meshes as well as evaluation of interface energy integrals. A preliminary version of this treatment was presented in [37]. That work did not cover, however, the use of the displacement potential as primary fluid variable nor modifications necessary for cavitation, silent boundaries and free surface slosh effects.

Since our focus is on the treatment of FSI, no LLM frame is placed at the soil–structure interface. Nothing precludes treating that interface as particular case of structure–structure interaction (SSI). Because this coupling has been previously studied, with emphasis on contact and friction effects [36], the development is not repeated here. Furthermore, to avoid interference with the FSI study, soil and structure are modeled by the same finite element program using matching meshes. Silent boundaries are needed, however, to account for truncation of the fluid and soil meshes, as illustrated in Fig. 2a.

3. Localized Lagrange multiplier method for FSI

The LLM treatment is based on a simple variational rule. The governing functional of the coupled system is that of the individual components plus their interaction:

$$\Pi_{\mathrm{T}} = \Pi_{\mathrm{F}} + \Pi_{\mathrm{S}} + \Pi_{\mathrm{B}}. \tag{1}$$

Here Π_{F} and Π_{S} are space–time functionals for the isolated fluid and structure, respectively. Π_{B} is a functional called the *interface potential* that accounts for the fluid–structure interface conditions. Setting $\delta\Pi_{\mathrm{T}} = 0$ yields the field equations, boundary and interface conditions as Euler–Lagrange equations. Upon space discretization of (1), the coupled semidiscrete equations are obtained by making Π_{T} stationary with respect to the selected degrees of freedom.

While Π_{F} and Π_{S} can be selected from an assortment of well known functionals (normally those used in existing codes for the structure and fluid alone), Π_{B} is constructed to yield the FSI conditions as Euler–Lagrange equations. The specific form depends on: (i) the chosen interface state variables, (ii) the kinematic and equilibrium conditions on the field variables (displacements, tractions) on either side of the interface, and (iii) interface constitutive assumptions such as energy dissipation, no-slip, friction, etc. These have been previously developed for SSI. For the nondissipative case, examples are provided in [36], whereas friction and hysteresis models are treated in [49]. For FSI, functional Π_{B} was introduced in [37] with displacement-based fluid models in mind but without specific applications. It is extended here to the displacement-potential treatment of acoustic fluids.

The LLM treatment of FSI is schematized in Figs. 3 and 4. These illustrate both matching and non-matching mesh scenarios. The interface frame serves as a force transducer device defined by its displacements $\mathbf{u}_{\mathrm{B}}$. The localized Lagrange multiplier fields λ_{F} and λ_{S} enforce interface compatibility between frame and fluid and frame and structure, respectively [37]. Multipliers are discretized as point forces

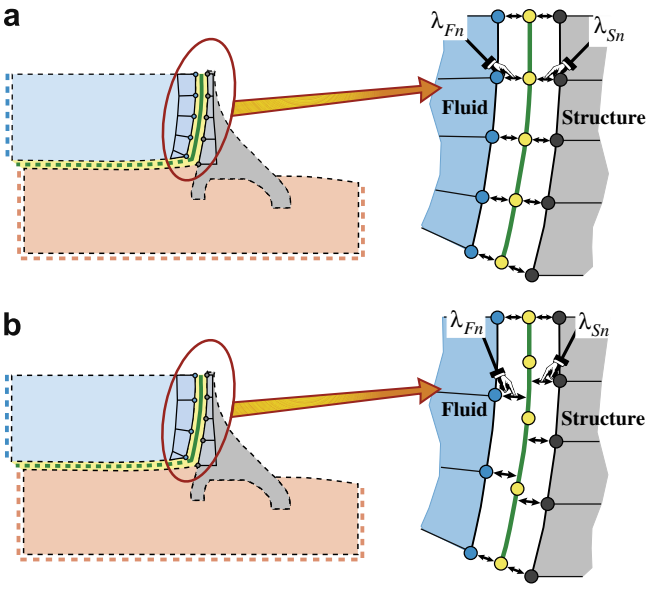

Fig. 3. Linking meshes with LLM treated interface: (a) matching meshes, (b) non-matching meshes. Only interface "wet nodes" are shown for clarity.

(delta functions) collocated at the nodes, as shown in that figure. No dissipation mechanisms, such as friction or boundary layers, are included in this model. Thermal effects are ignored.

Ensuing equations are expressed with respect to a rectangular Cartesian system x_i $(i = 1, 2, 3)$. Einstein's summation convention over repeated indices is adopted unless explicitly suppressed. Roman indices range over $1, 2, 3$ whereas Greek indices range over $1, 2$. Coordinates are often grouped in a column position vector $\mathbf{x}^{\mathrm{T}} = [x_1\ x_2\ x_3] = [x_i]$. Unit normal components are denoted by n_i $(i = 1, 2, 3)$, and collected into vector $\mathbf{n}^{\mathrm{T}} = [n_1\ n_2\ n_3] = [n_i]$. The spatial partial derivative abbreviation $(\cdot)_{,i} = \partial(\cdot)/\partial x_i$ is occasionally used. A superposed dot denotes time differentiation. A prime denotes derivative with respect to coordinate $x \equiv x_1$ in spatially one-dimensional problems. Coordinates are relabeled $x_1 \to x, x_2 \to y, x_3 \to z$ when appropriate.

3.1. Component functionals

The LLM formulation begins by partitioning the coupled system into individual subsystems, and choosing the energy functionals in (1). To facilitate software reuse, the choice for the fluid and structure is often limited to functionals in common use.

The primary variable for the structure in most finite element method (FEM) implementations is the displacement field. For expository expedience the structure functional is taken to be the total potential energy (TPE) functional. This is written below in d'Alembertian form with inertial and damping forces expressed as modified body forces.

$$\begin{aligned}\Pi_{\mathrm{S}} &= \Pi_{\mathrm{TPE}} \\ &= \frac{1}{2}\int_{\Omega_{\mathrm{S}}} \sigma_{ij}\epsilon_{ij}\,\mathrm{d}\Omega_{\mathrm{S}} - \int_{\Omega_{\mathrm{S}}} u_{\mathrm{S}i}(b_{\mathrm{S}i} - \rho_{\mathrm{S}}\ddot{u}_{\mathrm{S}i} - d_{\mathrm{S}}\dot{u}_{\mathrm{S}i})\mathrm{d}\Omega_{\mathrm{S}} \\ &\quad - \int_{\Gamma_{\mathrm{S}}} t_{\mathrm{S}i}u_{\mathrm{S}i}\,\mathrm{d}\Gamma_{\mathrm{S}} \\ &= \frac{1}{2}\int_{\Omega_{\mathrm{S}}} \epsilon_{ij}E_{ijk\ell}\epsilon_{k\ell}\,\mathrm{d}\Omega_{\mathrm{S}} - \int_{\Omega_{\mathrm{S}}} u_{\mathrm{S}i}(b_{\mathrm{S}i} - \rho_{\mathrm{S}}\ddot{u}_{\mathrm{S}i} \\ &\quad - d_{\mathrm{S}}\dot{u}_{\mathrm{S}i})\,\mathrm{d}\Omega_{\mathrm{S}} - \int_{\Gamma_{\mathrm{S}}} t_{\mathrm{S}i}u_{\mathrm{S}i}\,\mathrm{d}\Gamma_{\mathrm{S}}. \end{aligned} \tag{2}$$

Here subscript S refers to the structure, σ_{ij} and ϵ_{ij} denote the stress and strain tensors, respectively, $E_{ijk\ell}$ the elasticity tensor, u_i the displacements, b_i the body forces, ρ the mass density, d_{S} the structural damping per unit of volume, $t_{\mathrm{S}i}$ the surface tractions, Ω_{S} the structural domain and Γ_{S} the traction-specified structural boundary. Other functionals, such as Hellinger–Reissner, Veubeke–Hu–Washizu or Pian–Tong hybrids, could be selected as well. The only requirement is that they lead to elements with nodal displacement freedoms as connectors.

Choosing Π_{F} is less automatic. The acoustic fluid is modeled as compressible, irrotational, inviscid, of constant density, adiabatic and initially at rest. The constitutive equation that expresses the small compressibility of a liquid can be written [16,25,29]

$$p = -K\epsilon_V = -Ku_{\mathrm{F}i,i} = -\rho_{\mathrm{F}}c^2u_{\mathrm{F}i,i}. \tag{3}$$

Here subscript F refers to the fluid, p is the dynamic pressure (positive if compressive), K the bulk modulus (about 2.1 GPa in water), $\epsilon_V = \epsilon_{ii} = u_{\mathrm{F}i,i}$ the volumetric strain measured from hydrostatic equilibrium, and $c = \sqrt{K/\rho_{\mathrm{F}}}$ the speed of sound (about 1480 m/s in water). Three primary variable choices are possible: displacements, displacement potential, or pressure. To facilitate coupling with Π_{S} we initially pick the fluid displacements $u_{\mathrm{F}i}$ as the primary variables, subject to subsequent transformations to enforce irrotationality. Using (3) and conservation of energy the fluid functional emerges as

$$\begin{aligned}\Pi_{\mathrm{F}} = \frac{1}{2}\int_{\Omega_{\mathrm{F}}} \rho_{\mathrm{F}}c^2u_{\mathrm{F}i,i}u_{\mathrm{F}j,j}\,\mathrm{d}\Omega_{\mathrm{F}} - \int_{\Omega_{\mathrm{F}}} u_{\mathrm{F}i}(b_{\mathrm{F}i} - \rho_{\mathrm{F}}\ddot{u}_{\mathrm{F}i})\mathrm{d}\Omega_{\mathrm{F}} \\ - \int_{\Gamma_{\mathrm{F}}} t_{\mathrm{F}i}u_{\mathrm{F}i}\,\mathrm{d}\Gamma_{\mathrm{F}},\end{aligned} \tag{4}$$

where Ω_{F} is the fluid domain, Γ_{F} the traction-specified fluid boundary, and other terms are as in the structure functional.

The final ingredient is the interface functional Π_{B}. The procedure described in [36,37] is used as our starting point. Fluid and structure are separated at the fluid–structure boundary Γ_{B}, also known as the "wet surface", and an interface kinematic frame is inserted as illustrated in Fig. 2b. Frame displacements $u_{\mathrm{B}i}$ are introduced as addi-

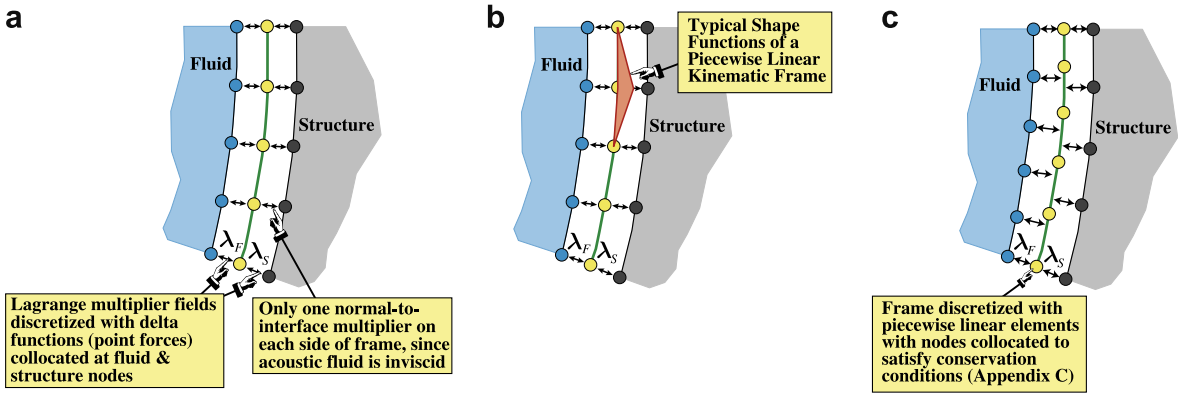

Fig. 4. LLM treatment details: (a and b) matching meshes, (c) non-matching meshes.

tional primary variables. In structure–structure interaction (SSI), compatibility of the boundary displacements is enforced with Lagrange multiplier (flux) fields, one on each frame side [36]. To take care of normal and tangential compatibility, such multipliers must have normal and tangential components. In our problem, however, the fluid is assumed to be inviscid and only normal displacements need to match. Denote by n_i the normal vector on the wet surface, conventionally selected to be exterior to the fluid. The appropriate form of the interface functional becomes

$$\Pi_{\mathrm{B}} = \int_{\Gamma_{\mathrm{FB}}} \lambda_{\mathrm{F}i} n_i (u_{\mathrm{F}i} n_i - u_{\mathrm{B}i} n_i) \mathrm{d}\Gamma_{\mathrm{FB}} + \int_{\Gamma_{\mathrm{SB}}} \lambda_{\mathrm{S}i} n_i (u_{\mathrm{S}i} n_i - u_{\mathrm{B}i} n_i) \mathrm{d}\Gamma_{\mathrm{SB}}. \tag{5}$$

Integration domains Γ_{FB} and Γ_{SB} denote boundaries between fluid and frame and between structure and frame, respectively. Often $\Gamma_{\mathrm{FB}} = \Gamma_{\mathrm{SB}}$, coincident with the structural wet surface. The total system functional Π_{T} of (1) is obtained by adding (2), (4) and (5).

3.2. Mortar interface treatment

Since its inception in 1990 [2] the Mortar method has gained popularity as a dual interfacing scheme for multiphysics capable of handling non-matched meshes. With growing use the name has come to designate a loosely related set of coupling techniques, most of them based on Galerkin or weighted residual methods; see e.g. [22]. In the context of this paper the term 'Mortar' is used in the sense of having *one* Lagrange multiplier field, denoted by λ_{B}, that directly links the fluid and structure interfaces (i.e. without a frame) within the variational framework of Eq. (1). The appropriate interface potential to be inserted there is

$$\Pi_{\mathrm{B}} = \int_{\Gamma_{\mathrm{B}}} \lambda_{\mathrm{B}} (u_{\mathrm{F}i} n_i - u_{\mathrm{S}i} n_i) \mathrm{d}\Gamma_{\mathrm{B}}, \tag{6}$$

in which λ_{B} is the primary interface variable. As discussed in [36], the source of this Π_{B} in solid mechanics can be traced back to Prager [42]. (An equivalent name for Mortar used in that reference is global Lagrange multiplier (GLM) method, to emphasize contrast to LLM.)

This interfacing technique was used in several of our application problems as verification and a calibration tool. To make a fair comparison, the multiplier space for λ_{B} also consists of node-collocated delta functions, as pictured in Fig. 5. While this choice is easy to implement for matching meshes, as shown in Fig. 5a, for non-matching meshes, cf. Fig. 5b, locating multipliers is not obvious. A common method is to declare one face as master, and collocate delta functions on the master nodes. This is pictured in Fig. 5c with the fluid face picked as master. Similar "master vs. slave" decisions may be necessary when using distributed Lagrange multiplier spaces. Regardless of which face is chosen as master, the master mesh must know about the boundary shape functions of the other, and the modularity of LLM is lost.

The equations of motion for the Mortar interface treatment are summarized in Appendix A as the starting point of the stability analysis of partitioned time integration.

3.3. Structure discretization

The structure is discretized by the usual procedures of the FEM. Assembly by the direct stiffness method (DSM) leads to the semidiscrete equations of motion

$$\mathbf{M}_{\mathrm{S}} \ddot{\mathbf{u}}_{\mathrm{S}} + \mathbf{C}_{\mathrm{S}} \dot{\mathbf{u}}_{\mathrm{S}} + \mathbf{K}_{\mathrm{S}} \mathbf{u}_{\mathrm{S}} = \mathbf{f}_{\mathrm{S}} - \mathbf{B}_{\mathrm{S}n} \boldsymbol{\lambda}_{\mathrm{S}}, \tag{7}$$

in which $\mathbf{M}_{\mathrm{S}}$, $\mathbf{C}_{\mathrm{S}}$ and $\mathbf{K}_{\mathrm{S}}$ are the master mass, damping and stiffness matrices, respectively, $\mathbf{u}_{\mathrm{S}}$ the vector of node displacements, $\mathbf{f}_{\mathrm{S}}$ the applied node force vector, $\boldsymbol{\lambda}_{\mathrm{S}}$ the vector of frame-to-structure interaction forces at wet structural nodes, and $\mathbf{B}_{\mathrm{S}n}$ is a "Boolean" matrix that maps $\boldsymbol{\lambda}_{\mathrm{S}}$ onto the full set of structural node forces. (These interaction forces are identified below with structure-to-frame Lagrange multipliers collocated at structure nodes, hence the symbol.) $\mathbf{B}_{\mathrm{S}n}$ is typically a highly sparse matrix.

3.4. Fluid discretization

The acoustic fluid is discretized in two stages. First a TPE-like, displacement-based functional such as (4) is chosen, element shape functions are assumed, and element equations in stiffness–mass form are obtained while ignor-

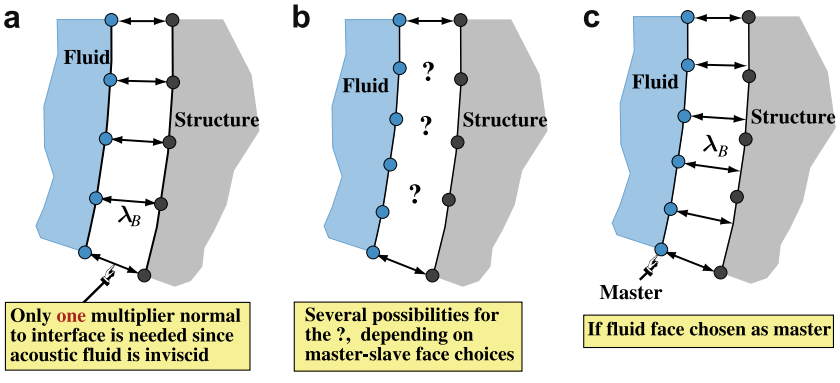

Fig. 5. Linking meshes with Mortar treated interface: (a) matching meshes, (b and c) non-matching meshes.

ing internal damping. For an individual acoustic fluid element identified by superscript e the displacement is expressed as $u^e_{\mathrm{F}i} = \mathbf{N}_{\mathrm{F}}\mathbf{u}^e_{\mathrm{F}i}$, where $\mathbf{N}_{\mathrm{F}}$ collects the element shape functions and $\mathbf{u}^e_{\mathrm{F}i}$ collects nodal values of the element in the ith direction. Applied forces include body forces collected in $\mathbf{b}_{\mathrm{F}}$ and surface tractions collected in $\mathbf{t}_{\mathrm{F}}$. The fluid element matrices are given by

$$\begin{aligned}
\mathbf{K}^e_{\mathrm{F}} &= \rho_{\mathrm{F}} c^2 \int_{\Omega^e_{\mathrm{F}}} (\nabla \mathbf{N}_{\mathrm{F}})^{\mathrm{T}} \nabla \mathbf{N}_{\mathrm{F}}\, \mathrm{d}\Omega_{\mathrm{F}},\\
\mathbf{M}^e_{\mathrm{F}} &= \rho_{\mathrm{F}} \int_{\Omega^e_{\mathrm{F}}} \mathbf{N}^{\mathrm{T}}_{\mathrm{F}} \mathbf{N}_{\mathrm{F}}\, \mathrm{d}\Omega_{\mathrm{F}},\\
\mathbf{f}^e_{\mathrm{F}} &= \int_{\Omega^e_{\mathrm{F}}} \mathbf{N}^{\mathrm{T}}_{\mathrm{F}} \mathbf{b}_{\mathrm{F}}\, \mathrm{d}\Omega_{\mathrm{F}} + \int_{\Gamma^e_{\mathrm{F}}} \mathbf{N}^{\mathrm{T}}_{\mathrm{F}} \mathbf{t}_{\mathrm{F}}\, \mathrm{d}\Gamma_{\mathrm{F}},
\end{aligned} \tag{8}$$

in which Ω^e_{F} and Γ^e_{F} denote fluid element volume and boundary, respectively, and ∇ the gradient operator. Assembly leads to the semidiscrete fluid equations of motion

$$\mathbf{M}_{\mathrm{F}}\ddot{\mathbf{u}}_{\mathrm{F}} + \mathbf{K}_{\mathrm{F}}\mathbf{u}_{\mathrm{F}} = \mathbf{f}_{\mathrm{F}} - \mathbf{B}_{\mathrm{F}n}\boldsymbol{\lambda}_{\mathrm{F}}. \tag{9}$$

Here $\mathbf{M}_{\mathrm{F}}$, $\mathbf{K}_{\mathrm{F}}$ and $\mathbf{f}_{\mathrm{F}}$ are the master mass matrix, stiffness matrix and applied force vector for the fluid, $\mathbf{u}_{\mathrm{F}}$ the fluid displacement vector, $\boldsymbol{\lambda}_{\mathrm{F}}$ the array of frame-to-fluid interaction forces at fluid nodes, and $\mathbf{B}_{\mathrm{F}n}$ a typically sparse Boolean matrix that maps $\boldsymbol{\lambda}_{\mathrm{F}}$ to the full set of fluid node forces. (Those interaction forces are identified below with frame-to-fluid Lagrange multipliers collocated at structure nodes, hence the symbol.)

In the second stage the matrix equations (9) are rewritten in terms of displacement potential variables to preclude circulation modes. This process is covered in Section 4.

3.5. LLM interface discretization

As outlined in the two foregoing subsections, use of the interface functional Π_{B} of (5) with varied multipliers and frame displacements allows the structure and fluid to be independently discretized by standard methods. The new ingredient is the discretization of Π_{B}. This requires decisions on finite element spaces for multipliers and frame displacements. Two choices proven useful in previous applications to SSI [38] are

(1) Multiplier fields are represented by delta functions collocated at nodes of the interacting subsystems. Physically those represent interaction point forces conjugate to node displacements.
(2) Frame displacements are discretized by piecewise linear or bilinear shape functions.

Choice (1) offers localization benefits: multiplier node values are applied directly to structure and fluid meshes through the interaction force terms $\mathbf{B}_{\mathrm{S}n}\boldsymbol{\lambda}_{\mathrm{S}}$ and $\mathbf{B}_{\mathrm{F}n}\boldsymbol{\lambda}_{\mathrm{F}}$, respectively, displayed in (7) and (9). As a result the structure program need not know anything about the fluid mesh, and vice-versa: at each time step those programs receive only node forces from the interface module. A second advantage is that computation of the integrals in Eq. (5) becomes trivial. The tradeoff is that placement of frame nodes in the case of non-matching meshes becomes a nontrivial task, as discussed later. If meshes match, frame nodes can be collocated directly at common nodes, as illustrated in Fig. 3a, and the process is considerably simplified.

Node collocation is expressed by relating multiplier shape functions to a Dirac delta distribution:

$$\begin{aligned}
&\lambda_{\mathrm{S}}(\mathbf{x}) = \mathbf{N}_{\lambda\mathrm{S}i}\boldsymbol{\lambda}_{\mathrm{S}i}, \quad \lambda_{\mathrm{F}}(\mathbf{x}) = \mathbf{N}_{\lambda\mathrm{F}j}\boldsymbol{\lambda}_{\mathrm{F}j} \quad \text{with}\\
&\mathbf{N}_{\lambda\mathrm{S}i} = \delta(\mathbf{x} - \mathbf{x}_{\lambda\mathrm{S}i}), \quad \mathbf{N}_{\lambda\mathrm{F}j} = \delta(\mathbf{x} - \mathbf{x}_{\lambda\mathrm{F}j}).
\end{aligned} \tag{10}$$

Here $\mathbf{x}_{\lambda\mathrm{S}i}$ is the position vector of the ith structural Lagrange multiplier on Γ_{SB} whereas $\mathbf{x}_{\lambda\mathrm{F}j}$ is the position vector for the jth fluid multiplier on Γ_{FB}. Integration over those surfaces reduces to evaluation at nodes [24], thus defining the Boolean matrices $\mathbf{B}_{\mathrm{S}n}$ and $\mathbf{B}_{\mathrm{F}n}$ of the semidiscrete equations of motion (7) and (9) according to the rules

$$\begin{aligned}
\int_{\Gamma_{\mathrm{SB}}} \lambda_{\mathrm{S}i} n_i u_{\mathrm{S}i} n_i\, \mathrm{d}\Gamma_{\mathrm{SB}} &\Rightarrow \boldsymbol{\lambda}^{\mathrm{T}}_{\mathrm{S}} \left[\int_{\Gamma_{\mathrm{SB}}} \mathbf{N}^{\mathrm{T}}_{\lambda\mathrm{S}} \mathbf{n}\mathbf{n}^{\mathrm{T}} \mathbf{N}_{\mathrm{S}}\, \mathrm{d}\Gamma_{\mathrm{SB}} \right] \mathbf{u}_{\mathrm{S}}\\
&\stackrel{\mathrm{def}}{=} \boldsymbol{\lambda}^{\mathrm{T}}_{\mathrm{S}} \mathbf{B}_{\mathrm{S}n}\mathbf{u}_{\mathrm{S}},\\
\int_{\Gamma_{\mathrm{FB}}} \lambda_{\mathrm{F}i} n_i u_{\mathrm{F}i} n_i\, \mathrm{d}\Gamma_{\mathrm{FB}} &\Rightarrow \boldsymbol{\lambda}^{\mathrm{T}}_{\mathrm{F}} \left[\int_{\Gamma_{\mathrm{FB}}} \mathbf{N}^{\mathrm{T}}_{\lambda\mathrm{F}} \mathbf{n}\mathbf{n}^{\mathrm{T}} \mathbf{N}_{\mathrm{F}}\, \mathrm{d}\Gamma_{\mathrm{FB}} \right] \mathbf{u}_{\mathrm{F}}\\
&\stackrel{\mathrm{def}}{=} \boldsymbol{\lambda}^{\mathrm{T}}_{\mathrm{F}} \mathbf{B}_{\mathrm{F}n}\mathbf{u}_{\mathrm{F}},
\end{aligned} \tag{11}$$

where $\mathbf{n} = [n_1 n_2 n_3]^{\mathrm{T}}$ is the exterior normal unit vector. Matrices $\mathbf{B}_{\mathrm{S}n}$ and $\mathbf{B}_{\mathrm{F}n}$ are typically sparse because the only nonzero entries, which are ± 1 under appropriate axes alignment at interface nodes, pertain to interface normal displacements. Thus they can be efficiently represented by pointer or marker arrays.

To discretize Π_{B} it is necessary to discretize the normal motion of the displacement frame. Frame node locations are determined through a technique termed the *zero-moment rule* [38], which is outlined in Appendix B. As a result those displacements are interpolated over frame elements by

$$u^e_{\mathrm{B}i} = \mathbf{N}_{\mathrm{B}}\mathbf{u}^e_{\mathrm{B}}, \tag{12}$$

where $\mathbf{N}_{\mathrm{B}}$ collects the element shape functions. Inserting this into Π_{B} along with the multiplier representation (10) the connection matrices $\mathbf{L}_{\mathrm{S}n}$ and $\mathbf{L}_{\mathrm{F}n}$ are defined according to the rules

$$\begin{aligned}
\int_{\Gamma_{\mathrm{B}}} \lambda_{\mathrm{S}i} n_i u_{\mathrm{B}i} n_i\, \mathrm{d}\Gamma_{\mathrm{B}} &\Rightarrow \boldsymbol{\lambda}^{\mathrm{T}}_{\mathrm{S}} \left[\int_{\Gamma_{\mathrm{B}}} \mathbf{N}^{\mathrm{T}}_{\lambda\mathrm{S}} \mathbf{n}\mathbf{n}^{\mathrm{T}} \mathbf{N}_{\mathrm{B}}\, \mathrm{d}\Gamma_{\mathrm{B}} \right] \mathbf{u}_{\mathrm{B}}\\
&\stackrel{\mathrm{def}}{=} \boldsymbol{\lambda}^{\mathrm{T}}_{\mathrm{S}} \mathbf{L}_{\mathrm{S}n}\mathbf{u}_{\mathrm{B}},\\
\int_{\Gamma_{\mathrm{B}}} \lambda_{\mathrm{F}i} n_i u_{\mathrm{B}i} n_i\, \mathrm{d}\Gamma_{\mathrm{B}} &\Rightarrow \boldsymbol{\lambda}^{\mathrm{T}}_{\mathrm{F}} \left[\int_{\Gamma_{\mathrm{B}}} \mathbf{N}^{\mathrm{T}}_{\lambda\mathrm{F}} \mathbf{n}\mathbf{n}^{\mathrm{T}} \mathbf{N}_{\mathrm{B}}\, \mathrm{d}\Gamma_{\mathrm{B}} \right] \mathbf{u}_{\mathrm{F}}\\
&\stackrel{\mathrm{def}}{=} \boldsymbol{\lambda}^{T}_{\mathrm{F}} \mathbf{L}_{\mathrm{F}n}\mathbf{u}_{\mathrm{B}}.
\end{aligned} \tag{13}$$

Because of the presence of the delta functions in $\mathbf{N}_{\lambda\mathrm{S}}$ and $\mathbf{N}_{\lambda\mathrm{F}}$, the integration reduces to evaluation of the frame interpolation function, projected on the interface exterior normal, at

locations of the structure and fluid interface nodes. Detailed examples for SSI applications may be found in [38].

For non-matching meshes, $\mathbf{L}_{Sn}$ and $\mathbf{L}_{Fn}$ connect multiplier forces on both sides of Γ_B. In the particular case of matching meshes with interface-normal aligned axes, those become Boolean matrices. Connection matrices are typically sparse and appropriate formats should be used to take advantage of that property in production codes.

The solution interface error may be reduced if the Lagrange multiplier shape functions are piecewise-linearly interpolated over frame elements [13]. The tradeoff is that spatial integration of the interface potential becomes substantially more complicated, especially in three dimensions.

For future use the discretized version of the total functional (1) can be expressed as

$$\begin{aligned}\Pi_T = {} & \mathbf{u}_S^T\left(\frac{1}{2}\mathbf{K}_S\mathbf{u}_S + \mathbf{C}_S\dot{\mathbf{u}}_S + \mathbf{M}_S\ddot{\mathbf{u}}_S - \mathbf{f}_S\right) \\ & + \mathbf{u}_F^T\left(\frac{1}{2}\mathbf{K}_F\mathbf{u}_F + \mathbf{M}_F\ddot{\mathbf{u}}_F - \mathbf{f}_F\right) + \boldsymbol{\lambda}_S^T(\mathbf{B}_{Sn}^T\mathbf{u}_S \\ & - \mathbf{L}_{Sn}\mathbf{u}_B) + \boldsymbol{\lambda}_F^T(\mathbf{B}_{Fn}^T\mathbf{u}_F - \mathbf{L}_{Fn}\mathbf{u}_B). \end{aligned} \tag{14}$$

4. Linkage to fluid displacement potential

The acoustic fluid equations have been initially expressed in terms of fluid displacements to simplify coupling to the structure through the LLM frame. This choice, however, brings on a serious computational difficulty: the appearance of spurious kinematic modes. Since an acoustic fluid is irrotational and inviscid, its internal energy responds only to volumetric changes. As a result, displacement-based elements can become highly rank deficient.

As an example, consider an 8-node, 24 degree-of-freedom, displacement-assumed fluid brick element with regular (cubic-like) geometry. Under exact integration (or, equivalently, Gauss rules $2\times2\times2$ or higher) the fluid stiffness matrix $\mathbf{K}_F$ displays seven volumetric modes and six rigid-body modes, leaving $24-7-6=11$ spurious modes. If a reduced one-point integration is used, only three volumetric modes are captured, leaving $24-3-6=15$ spurious modes. These are commonly called *circulation modes* or *rotational modes* in the FEM literature [23]. Since circulation modes can propagate through a mesh, a direct time integration response calculation or a frequency analysis can be completely ruined. Two methods have been proposed to deal with this problem:

(1) Keep displacements as primary variables, but enforce irrotationality by a penalty method.
(2) Use a scalar primary variable field that automatically enforces irrotationality. Three possible choices are the pressure p, displacement potential ψ and velocity potential φ.

Hamdi and Ousset [20] as well as Wilson and Khalvati [48] favored the penalty treatment by applying irrotationality constraints that force circulation modes to absorb energy, hoping that only low frequency modes would be excited. This hope was realized in the problems considered in those references. However, in irregular meshes circulation modes may in fact display nonzero frequency due to the use of full integration in the mass matrix, leading to mode identification problems. To address these issues the concurrent use of the penalty method and a projected mass matrix was proposed in [6,23]. This allowed for the retention of low frequency modes while removing the spurious modes. In the cases studied in [23] low frequency modes were attributed to the effect of sloshing. Unfortunately, this method is complicated and requires iteration to determine appropriate penalty values [48].

The second approach precludes circulation modes once and for all and has the additional benefit of requiring only one freedom per fluid node, reducing the number of fluid freedoms by half in 2D and by two-thirds in 3D. The downside is that coupling with displacements is not simple. Of the choices listed above, in the late 1970s Newton systematically compared the displacement potential and pressure formulations [30–33]. While little difference was found in linear problems, the former proved superior when cavitation was considered. Accordingly this formulation was favored by Felippa and DeRuntz [15], Zienkiewicz et al. [50], and Sprague and Geers [47] for simulation of strong shocks that could trigger hull cavitation near underwater vehicles, or bulk cavitation under surface ships. This choice was adopted in this study.

4.1. The fluid gradient matrix

The fluid displacement potential field $\psi=\psi(x_i,t)$ is a scalar function of space and time that generates the displacement field as its gradient: $\vec{\mathbf{u}}=\nabla\psi$ or in index form, $u_i=\partial\psi/\partial x_i$. This field is automatically irrotational since $\nabla\times\vec{\mathbf{u}}=\nabla\times\nabla\psi=0$.

To fix ideas, consider the 4-node quadrilateral displacement-potential-based fluid element pictured in Fig. 6. The geometry is defined in terms of the usual natural coordinates ξ and η, as shown in Fig. 6a. The element has four degrees of freedom, which are the displacement potentials ψ_i at the corners $i=1,2,3,4$, as illustrated in Fig. 6b.

To reduce subscripting clutter, in this section coordinates will be denoted by x and y instead of x_1 and x_2, respectively, with (x_i,y_i) as coordinates of node i. Both

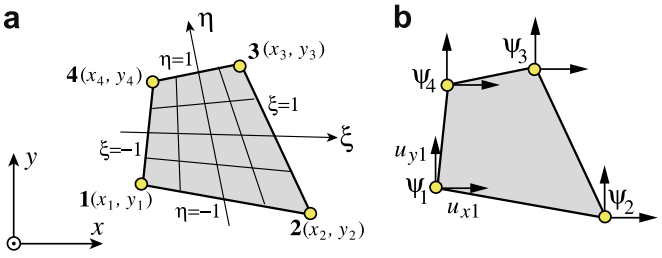

Fig. 6. A 4-node displacement-potential 2D fluid element.

(x, y) and the displacement potential ψ are interpolated isoparametrically:

$$\begin{bmatrix} 1 \\ x \\ y \\ \psi \end{bmatrix} = \begin{bmatrix} 1 & 1 & 1 & 1 \\ x_1 & x_2 & x_3 & x_4 \\ y_1 & y_2 & y_3 & y_4 \\ \psi_1 & \psi_2 & \psi_3 & \psi_4 \end{bmatrix} \begin{bmatrix} N_1 \\ N_2 \\ N_3 \\ N_4 \end{bmatrix}, \tag{15}$$

with the bilinear shape functions $N_1 = \frac{1}{4}(1-\xi)(1-\eta)$, $N_2 = \frac{1}{4}(1+\xi)(1-\eta)$, $N_3 = \frac{1}{4}(1+\xi)(1+\eta)$ and $N_4 = \frac{1}{4}(1-\xi)(1+\eta)$. Corner coordinate differences are abbreviated as $x_{ij} = x_i - x_j$ and $y_{ij} = y_i - y_j$. The Jacobian determinant is $J = \frac{1}{4}(A + A_1\xi + A_2\eta)$ where $A = \frac{1}{2}(x_{31}y_{42} - x_{42}y_{31})$ is the area of the quadrilateral, $A_1 = \frac{1}{2}(x_{34}y_{12} - x_{12}y_{34})$ and $A_2 = \frac{1}{2}(x_{23}y_{14} - x_{14}y_{23})$.

In terms of the node displacement 4-vector $\boldsymbol{\psi}^e = [\psi_1 \;\; \psi_2 \;\; \psi_3 \;\; \psi_4]^{\mathrm{T}}$ the Cartesian gradients $u_x = \partial\psi/\partial x$ and $u_y = \partial\psi/\partial y$ are given by

$$\begin{bmatrix} u_x \\ u_y \end{bmatrix} = \frac{1}{8J}\left(\begin{bmatrix} y_{24} & y_{31} & y_{42} & y_{13} \\ x_{42} & x_{13} & x_{24} & x_{31} \end{bmatrix} + \begin{bmatrix} y_{43} & y_{34} & y_{12} & y_{21} \\ x_{34} & x_{43} & x_{21} & x_{12} \end{bmatrix}\xi + \begin{bmatrix} y_{32} & y_{14} & y_{41} & y_{23} \\ x_{23} & x_{41} & x_{14} & x_{32} \end{bmatrix}\eta \right)\boldsymbol{\psi}^e. \tag{16}$$

Evaluating (16) at the nodes yields

$$\mathbf{u}_{\mathrm{F}}^e = \begin{bmatrix} u_{x1} \\ u_{y1} \\ u_{x2} \\ u_{y2} \\ u_{x3} \\ u_{y3} \\ u_{x4} \\ u_{y4} \end{bmatrix} = \frac{1}{4}\begin{bmatrix} y_{24}/J_1 & y_{41}/J_1 & 0 & y_{12}/J_1 \\ x_{42}/J_1 & x_{14}/J_1 & 0 & x_{21}/J_1 \\ y_{23}/J_2 & y_{31}/J_2 & y_{12}/J_2 & 0 \\ x_{32}/J_2 & x_{13}/J_2 & x_{21}/J_2 & 0 \\ 0 & y_{34}/J_3 & y_{42}/J_3 & y_{23}/J_3 \\ 0 & x_{43}/J_3 & x_{24}/J_3 & x_{32}/J_3 \\ y_{34}/J_4 & 0 & y_{41}/J_4 & y_{13}/J_4 \\ x_{43}/J_4 & 0 & x_{14}/J_4 & x_{31}/J_4 \end{bmatrix} \begin{bmatrix} \psi_1 \\ \psi_2 \\ \psi_3 \\ \psi_4 \end{bmatrix} = \mathbf{D}^e\boldsymbol{\psi}^e, \tag{17}$$

in which J_i are the corner Jacobians. These can be rapidly calculated from

$$\begin{aligned} 4J_1 &= A - A_1 - A_2 = x_{14}y_{21} - x_{21}y_{14} = x_{42}y_{14} - x_{14}y_{42}, \\ 4J_2 &= A + A_1 - A_2 = x_{21}y_{32} - x_{32}y_{21} = x_{13}y_{21} - x_{21}y_{13}, \\ 4J_3 &= A + A_1 + A_2 = x_{32}y_{43} - x_{43}y_{32} = x_{24}y_{32} - x_{32}y_{24}, \\ 4J_4 &= A - A_1 + A_2 = x_{43}y_{14} - x_{14}y_{43} = x_{31}y_{43} - x_{43}y_{31}. \end{aligned} \tag{18}$$

The 8×4 gradient matrix $\mathbf{D}^e$ relates the Cartesian node displacement components to the node displacement potentials. A similar transformation $\mathbf{u}_{\mathrm{F}}^e = \mathbf{D}^e\boldsymbol{\psi}^e$ can be constructed for any fluid element geometry based on the displacement potential element by appropriate differentiation and evaluation at nodes. For the assembled fluid system, the transformation reads $\mathbf{u}_{\mathrm{F}} = \mathbf{D}_{\mathrm{F}}\boldsymbol{\psi}$, where the entries of $\mathbf{D}_{\mathrm{F}}$ are obtained by averaging over node patching. Performing the change of basis $\mathbf{u}_{\mathrm{F}} \Rightarrow \boldsymbol{\psi}$ by a congruent transformation, the fluid energy is expressed in terms of $\boldsymbol{\psi}$ as energy gives

$$\begin{aligned} \Pi_{\mathrm{F}} &= \frac{1}{2}\boldsymbol{\psi}^{\mathrm{T}}\mathbf{D}_{\mathrm{F}}^{\mathrm{T}}\mathbf{K}_{\mathrm{F}}\mathbf{D}_{\mathrm{F}}\boldsymbol{\psi} + \frac{1}{2}\ddot{\boldsymbol{\psi}}^{\mathrm{T}}\mathbf{D}^{\mathrm{T}}\mathbf{M}_{\mathrm{F}}\mathbf{D}\ddot{\boldsymbol{\psi}} - \boldsymbol{\psi}^{\mathrm{T}}\mathbf{D}^{\mathrm{T}}\mathbf{f}_{\mathrm{F}} \\ &= \frac{1}{2}\boldsymbol{\psi}^{\mathrm{T}}\mathbf{K}_{\mathrm{F}\psi}\boldsymbol{\psi} + \frac{1}{2}\ddot{\boldsymbol{\psi}}^{\mathrm{T}}\mathbf{M}_{\mathrm{F}\psi}\ddot{\boldsymbol{\psi}} - \boldsymbol{\psi}^{\mathrm{T}}\mathbf{f}_{\mathrm{F}\psi}, \quad \text{in which} \\ \mathbf{M}_{\mathrm{F}\psi} &= \mathbf{D}_{\mathrm{F}}^{\mathrm{T}}\mathbf{M}_{\mathrm{F}}\mathbf{D}_{\mathrm{F}}, \quad \mathbf{K}_{\mathrm{F}\psi} = \mathbf{D}_{\mathrm{F}}^{\mathrm{T}}\mathbf{K}_{\mathrm{F}}\mathbf{D}_{\mathrm{F}}, \quad \mathbf{f}_{\mathrm{F}\psi} = \mathbf{D}_{\mathrm{F}}^{\mathrm{T}}\mathbf{f}_{\mathrm{F}}. \end{aligned} \tag{19}$$

The application of $\mathbf{D}_{\mathrm{F}}$ through a congruent transformation is equivalent to projecting the master stiffness, mass and force onto the subspace of irrotational fluid motions. The process is systematic and avoids the use of trial-and-error penalty devices.

4.2. Stabilization of surface-wave modes

In using the foregoing projection scheme circulation modes are eliminated. If the fluid has a free surface, as in the driver application problem of Fig. 1, there remain zero energy modes associated with sloshing (gravity waves) as pointed out in [48]. These can be converted to finite frequency modes by incorporating a gravity-potential energy functional in the derivations [16,29]. This is done by modifying the pressure on the free surface $\Gamma_{\mathrm{F}s}$ to be $p_{\mathrm{F}s}(x_i, t) = p_{\mathrm{atm}} - \rho_{\mathrm{F}} g_n u_n(x_i, t)$, in which p_{atm} is the atmospheric pressure, g_n the acceleration of gravity along the unit normal n_i, and u_n the displacement normal to $\Gamma_{\mathrm{F}s}$. In the present formulation that modification is done by taking $-\rho_{\mathrm{F}} g_n u_n$ as a surface traction term working on the normal displacement u_n, thus producing a potential $\frac{1}{2}\rho_{\mathrm{F}} g_n u_n^2$ per unit area. Interpolation by fluid-displacement shape functions and integration over $\Gamma_{\mathrm{F}s}$ creates an additional "sloshing stiffness" term that contributes to free-surface fluid nodes. The additional stiffness is given by

$$\mathbf{K}_{\mathrm{F}s} = \int_{\Gamma_{\mathrm{F}s}} \rho_{\mathrm{F}} g_n \mathbf{N}_{\mathrm{F}}^{\mathrm{T}}\mathbf{n}\mathbf{n}^{\mathrm{T}}\mathbf{N}_{\mathrm{F}}\, \mathrm{d}\Gamma_{\mathrm{F}s}. \tag{20}$$

This is added to $\mathbf{K}_{\mathrm{F}}$ and transformed via (19) to displacement potential node freedoms. If the fluid is fully contained, as in a piston problem, this term vanishes. It may also be ignored in the case of rapid transients (e.g. underwater explosions) that would not excite low-frequency sloshing motions over the simulation time span of interest.

5. LLM Coupled equations of motion

Taking the first variation of (14) with fluid matrices expressed in terms of displacement potential freedoms as per (19) gives

$$\begin{aligned} \delta\Pi_{\mathrm{T}}(\mathbf{u}_{\mathrm{S}}, \boldsymbol{\psi}, \boldsymbol{\lambda}_{\mathrm{S}}, \boldsymbol{\lambda}_{\mathrm{F}}, \mathbf{u}_{\mathrm{B}}) = {} & \delta\mathbf{u}_{\mathrm{S}}^{\mathrm{T}}(\mathbf{M}_{\mathrm{S}}\ddot{\mathbf{u}}_{\mathrm{S}} + \mathbf{C}_{\mathrm{S}}\dot{\mathbf{u}}_{\mathrm{S}} + \mathbf{K}_{\mathrm{S}}\mathbf{u}_{\mathrm{S}} \\ & + \mathbf{B}_{\mathrm{S}n}\boldsymbol{\lambda}_{\mathrm{S}} - \mathbf{f}_{\mathrm{S}}) + \delta\boldsymbol{\psi}^{\mathrm{T}}(\mathbf{M}_{\mathrm{F}\psi}\ddot{\boldsymbol{\psi}} \\ & + \mathbf{K}_{\mathrm{F}\psi}\boldsymbol{\psi} + \mathbf{D}_{\mathrm{F}}^{\mathrm{T}}\mathbf{B}_{\mathrm{F}n}\boldsymbol{\lambda}_{\mathrm{F}} - \mathbf{D}_{\mathrm{F}}^{\mathrm{T}}\mathbf{f}_{\mathrm{F}}) \\ & + \delta\boldsymbol{\lambda}_{\mathrm{S}}^{\mathrm{T}}(\mathbf{B}_{\mathrm{S}n}^{\mathrm{T}}\mathbf{u}_{\mathrm{S}} - \mathbf{L}_{\mathrm{S}n}\mathbf{u}_{\mathrm{B}}) \\ & + \delta\boldsymbol{\lambda}_{\mathrm{F}}^{\mathrm{T}}(\mathbf{B}_{\mathrm{F}n}^{\mathrm{T}}\mathbf{D}_{\mathrm{F}}\boldsymbol{\psi} - \mathbf{L}_{\mathrm{F}n}\mathbf{u}_{\mathrm{B}}) \\ & + \delta\mathbf{u}_{\mathrm{B}}^{\mathrm{T}}(-\mathbf{L}_{\mathrm{S}n}^{\mathrm{T}}\boldsymbol{\lambda}_{\mathrm{S}} - \mathbf{L}_{\mathrm{F}n}^{\mathrm{T}}\boldsymbol{\lambda}_{\mathrm{F}}). \end{aligned} \tag{21}$$

Setting this variation to zero gives the coupled, semidiscrete equations of motion:

$$\begin{bmatrix} \mathbf{M}_S & \mathbf{0} & \mathbf{0} & \mathbf{0} & \mathbf{0} \\ \mathbf{0} & \mathbf{M}_{F\psi} & \mathbf{0} & \mathbf{0} & \mathbf{0} \\ \mathbf{0} & \mathbf{0} & \mathbf{0} & \mathbf{0} & \mathbf{0} \\ \mathbf{0} & \mathbf{0} & \mathbf{0} & \mathbf{0} & \mathbf{0} \\ \mathbf{0} & \mathbf{0} & \mathbf{0} & \mathbf{0} & \mathbf{0} \end{bmatrix} \begin{Bmatrix} \ddot{\mathbf{u}}_S \\ \ddot{\boldsymbol{\psi}} \\ \ddot{\boldsymbol{\lambda}}_S \\ \ddot{\boldsymbol{\lambda}}_F \\ \ddot{\mathbf{u}}_B \end{Bmatrix} + \begin{bmatrix} \mathbf{C}_S & \mathbf{0} & \mathbf{0} & \mathbf{0} & \mathbf{0} \\ \mathbf{0} & \mathbf{0} & \mathbf{0} & \mathbf{0} & \mathbf{0} \\ \mathbf{0} & \mathbf{0} & \mathbf{0} & \mathbf{0} & \mathbf{0} \\ \mathbf{0} & \mathbf{0} & \mathbf{0} & \mathbf{0} & \mathbf{0} \\ \mathbf{0} & \mathbf{0} & \mathbf{0} & \mathbf{0} & \mathbf{0} \end{bmatrix} \times \begin{Bmatrix} \dot{\mathbf{u}}_S \\ \dot{\boldsymbol{\psi}} \\ \dot{\boldsymbol{\lambda}}_S \\ \dot{\boldsymbol{\lambda}}_F \\ \dot{\mathbf{u}}_B \end{Bmatrix} + \begin{bmatrix} \mathbf{K}_S & \mathbf{0} & \mathbf{B}_{Sn} & \mathbf{0} & \mathbf{0} \\ \mathbf{0} & \mathbf{K}_{F\psi} & \mathbf{0} & \mathbf{D}_F^{\mathrm{T}}\mathbf{B}_{Fn} & \mathbf{0} \\ \mathbf{B}_{Sn}^{\mathrm{T}} & \mathbf{0} & \mathbf{0} & \mathbf{0} & -\mathbf{L}_{Sn} \\ \mathbf{0} & \mathbf{B}_{Fn}^{\mathrm{T}}\mathbf{D}_F & \mathbf{0} & \mathbf{0} & -\mathbf{L}_{Fn} \\ \mathbf{0} & \mathbf{0} & -\mathbf{L}_{Sn}^{\mathrm{T}} & -\mathbf{L}_{Fn}^{\mathrm{T}} & \mathbf{0} \end{bmatrix} \times \begin{Bmatrix} \mathbf{u}_S \\ \boldsymbol{\psi} \\ \boldsymbol{\lambda}_S \\ \boldsymbol{\lambda}_F \\ \mathbf{u}_B \end{Bmatrix} = \begin{Bmatrix} \mathbf{f}_S \\ \mathbf{D}_F^{\mathrm{T}}\mathbf{f}_F \\ \mathbf{0} \\ \mathbf{0} \\ \mathbf{0} \end{Bmatrix}. \tag{22}$$

This is not a conventional ordinary differential equation (ODE) system, but a differential–algebraic equation (DAE) of index 2 [5]. The first two matrix equations state discrete force equilibrium for the structure and fluid partition, respectively. The third and fourth equations represent interface compatibility conditions weakly enforced through the Lagrange multipliers. The last equation expresses Newton's third law at the interface frame. A slight generalization consists of allowing external forces $\mathbf{f}_B$ to be applied directly on interface frame nodes; if so, the last entry of the right-hand side vector would be replaced by $\mathbf{f}_B$.

6. Partitioned time integration

The semidiscrete equations of motion (22) are directly integrated in time using a partitioned analysis procedure conceptually based on [37,38]. (Direct integration is preferred over modal analysis to retain ability to do nonlinear problems.) The equations for the fluid, structure and interface partitions are processed separately. At each time step, interface equations receive vector information from the interacting systems and are algebraically solved for frame accelerations and Lagrange multipliers. The latter are broadcast to the fluid and structure partitions to update displacements and displacement potentials for the next step. Any convenient solver for the fluid and structure partitions may be used, and need not be the same.

The time integrator chosen is the Newmark method, which is widely used in earthquake engineering simulations [7,8,21]. Its generic expression is

$$\begin{aligned} \mathbf{u}^{n+1} &= \mathbf{u}^n + \Delta t\dot{\mathbf{u}}^{n+1} + \frac{1}{2}(\Delta t)^2[2\beta\ddot{\mathbf{u}}^{n+1} + (1-2\beta)\ddot{\mathbf{u}}^n], \\ \dot{\mathbf{u}}^{n+1} &= \dot{\mathbf{u}}^n + \Delta t[\gamma\ddot{\mathbf{u}}^{n+1} + (1-\gamma)\ddot{\mathbf{u}}^n]. \end{aligned} \tag{23}$$

Here n and $n+1$ denote the current and next time step index, respectively, $\Delta t = t^{n+1} - t^n$ the time stepsize, while β and γ are parameters that determine stability and accuracy characteristics. For simplicity in linear problems (β, γ) are often taken to be the same for both fluid ($\mathbf{u} \equiv \boldsymbol{\psi}$) and structure ($\mathbf{u} \equiv \mathbf{u}_S$).

When (23) is used to integrate a conventional second-order, linear ODE system monolithically (that is, without partitioning), it is well known (see e.g. [21]) that A-stability requires $\gamma \geqslant 1/2$ and $2\beta \geqslant \gamma$, whereas global second-order accuracy is achieved if $\gamma = 1/2$. Appendix A shows that those conditions also hold for both Mortar and LLM partitioned integration methods as presented here. Along with $\gamma = 1/2$, popular choices for β are 1/4, 1/6, 1/12 and 0, which pertain to instances known as the Trapezoidal Rule (TR), Linear Acceleration, Fox–Goodwin and Central Difference, respectively. Of these only TR (also called Average Acceleration in the Newmark context) is A-stable.

Suppose computations have proceeded until $t = t^n$. On inserting (23) into the first two matrix equations of (22) and moving next-step accelerations to the left side yields

$$\widehat{\mathbf{K}}_S\ddot{\mathbf{u}}_S^{n+1} = \mathbf{g}_S^{n+1} - \mathbf{B}_{Sn}\boldsymbol{\lambda}_S^{n+1}, \quad \widehat{\mathbf{K}}_F\ddot{\boldsymbol{\psi}}^{n+1} = \mathbf{g}_F^{n+1} - \mathbf{D}_F^{\mathrm{T}}\mathbf{B}_{Fn}\boldsymbol{\lambda}_F^{n+1}, \tag{24}$$

in which

$$\begin{aligned} \widehat{\mathbf{K}}_S &= \mathbf{M}_S + \Delta t\gamma\mathbf{C}_S + (\Delta t)^2\beta\mathbf{K}_S, \quad \widehat{\mathbf{K}}_F = \mathbf{M}_{F\psi} + (\Delta t)^2\beta\mathbf{K}_{F\psi}, \\ \mathbf{g}_S^{n+1} &= \mathbf{f}_S^{n+1} - \mathbf{C}_S[\dot{\mathbf{u}}_S^n + \Delta t(1-\gamma)\ddot{\mathbf{u}}_S^n] \\ &\quad - \mathbf{K}_S\left[\mathbf{u}_S^n + \Delta t\dot{\mathbf{u}}_S^n + \frac{1}{2}(\Delta t)^2(1-2\beta)\ddot{\mathbf{u}}_S^n\right], \\ \mathbf{g}_F^{n+1} &= \mathbf{D}_F^{\mathrm{T}}\mathbf{f}_F^{n+1} - \mathbf{K}_{F\psi}\left[\boldsymbol{\psi}^n + \Delta t\dot{\boldsymbol{\psi}}^n + \frac{1}{2}(\Delta t)^2(1-2\beta)\ddot{\boldsymbol{\psi}}^n\right]. \end{aligned} \tag{25}$$

The dynamic force vectors $\mathbf{g}_S^{n+1}$ and $\mathbf{g}_F^{n+1}$ are known quantities because they depend on past values and the next-step force. The dynamic stiffness matrices $\widehat{\mathbf{K}}_S$ and $\widehat{\mathbf{K}}_F$ are assumed to be nonsingular. To set up the interface equations, $\ddot{\mathbf{u}}_S^{n+1}$ and $\ddot{\boldsymbol{\psi}}^{n+1}$ are solved from (24) and substituted in the third and fourth matrix equations (the weak interface compatibility conditions) of (22) evaluated at $t = t^{n+1}$. For brevity introduce $\mathbf{G}_S = \mathbf{B}_{Sn}^{\mathrm{T}}\widehat{\mathbf{K}}_S^{-1}$, $\mathbf{G}_F = \mathbf{B}_{Fn}^{\mathrm{T}}\mathbf{D}_F\widehat{\mathbf{K}}_F^{-1}$, $\mathbf{P}_S = \mathbf{B}_{Sn}^{\mathrm{T}}\widehat{\mathbf{K}}_S^{-1}\mathbf{B}_{Sn} = \mathbf{G}_S\mathbf{B}_{Sn}$, and $\mathbf{P}_F = \mathbf{B}_{Fn}^{\mathrm{T}}\mathbf{D}_F\widehat{\mathbf{K}}_F^{-1}\mathbf{D}_F^{\mathrm{T}}\mathbf{B}_{Fn} = \mathbf{G}_F\mathbf{D}_F^{\mathrm{T}}\mathbf{B}_{Fn}$. The matrix compatibility equations become

$$\mathbf{P}_S\boldsymbol{\lambda}_S^{n+1} + \mathbf{L}_{Sn}\ddot{\mathbf{u}}_B^{n+1} = \mathbf{G}_S\mathbf{g}_S^{n+1}, \quad \mathbf{P}_F\boldsymbol{\lambda}_F^{n+1} + \mathbf{L}_{Fn}\ddot{\mathbf{u}}_B^{n+1} = \mathbf{G}_F\mathbf{g}_F^{n+1}. \tag{26}$$

Appending the sign-reverted last matrix equation of (22), evaluated at $t = t^{n+1}$, to the foregoing ones the following algebraic system emerges:

$$\begin{bmatrix} \mathbf{P}_S & \mathbf{0} & \mathbf{L}_{Sn} \\ \mathbf{0} & \mathbf{P}_F & \mathbf{L}_{Fn} \\ \mathbf{L}_{Sn}^{\mathrm{T}} & \mathbf{L}_{Fn}^{\mathrm{T}} & \mathbf{0} \end{bmatrix} \begin{Bmatrix} \boldsymbol{\lambda}_S^{n+1} \\ \boldsymbol{\lambda}_F^{n+1} \\ \ddot{\mathbf{u}}_B^{n+1} \end{Bmatrix} = \begin{Bmatrix} \mathbf{G}_S\mathbf{g}_S^{n+1} \\ \mathbf{G}_F\mathbf{g}_F^{n+1} \\ \mathbf{0} \end{Bmatrix}. \tag{27}$$

This will be referred to as the *interface equation*. It connects freedoms on Γ_B, and in 2D and 3D production problems it

typically has a small dimension compared to that of the fluid and structure state vectors. Although matrix inverses are shown for notational simplicity, in an actual implementation $\widehat{\mathbf{K}}_{\mathrm{S}}$ and $\widehat{\mathbf{K}}_{\mathrm{F}}$ are factored and solved for multiple right-hand sides while forming $\mathbf{P}_{\mathrm{S}}$ and $\mathbf{P}_{\mathrm{F}}$. In linear problems this is done only if Δt changes. Similarly, the "arrowhead" coefficient matrices in (27) need to be refactored only when $\mathbf{P}_{\mathrm{S}}$ and/or $\mathbf{P}_{\mathrm{F}}$ change.

To carry out the transient response, multipliers $\boldsymbol{\lambda}_{\mathrm{S}}^{n+1}$ and $\boldsymbol{\lambda}_{\mathrm{F}}^{n+1}$ are solved from (27). (The frame acceleration $\ddot{\mathbf{u}}_{\mathrm{B}}^{n+1}$, which appears as "multiplier glue" in (27), is also obtained as a byproduct but not needed for subsystem computations.) Multipliers are inserted into (24) to get $\ddot{\mathbf{u}}_{\mathrm{S}}^{n+1}$ and $\ddot{\boldsymbol{\psi}}^{n+1}$, and displacements and velocities are updated through (23). Since the fluid and structure systems become fully uncoupled upon solving the interface equation, different solvers and integration methods may be used if appropriate. Furthermore the two solutions may be done in parallel on a multiprocessing computer. The process is repeated until the simulation time span of interest is covered. Fig. 7 flowcharts the time-stepping procedure.

For problems involving "hard" local nonlinearities, such as fluid cavitation or structural fracture, an explicit integrator may be attractive for the partition that exhibits nonlinearities. The Central Difference (CD) form of (23) given by $\beta = 0$ and $\gamma = 1/2$ is explicit but as the analysis of Appendix A shows, unstable if used on both partitions.

A notable difference of this time-stepping scheme with respect to conventional staggered procedures is that *there is no explicit localized predictor* that directly transfers information from one partition to the other. Prediction is replaced by the solution of the interface equation. This injects coupling implicitness. As a result the Newmark A-stability with $(\gamma \geqslant 1/2, 2\beta \geqslant \gamma)$ is preserved. However, care must be taken in solving (27), because it can be ill-conditioned. To alleviate this concern, the interface equation may be scaled as described in [45].

7. Silent boundaries

In applications such as the dam problem of Fig. 1, fluid and solid silent boundaries (SB) are necessary to account for truncation of fluid and soil meshes to finite extent. Their locations are sketched in Fig. 2. Ideally a SB should radiate outgoing waves of arbitrary incident angles with no spurious reflections. This section focuses on the SB implementation for the fluid mesh, since the dual use of fluid displacements and their potential brings in some novel derivation points. The soil SB is directly selected from the available geotechnical literature.

The perfectly matched layer (PML) method [1] is generally considered the most accurate SB for computational acoustics and electromagnetics done in the frequency domain. Work has been recently done to extend it to the time domain [43]. For the application problems considered in the present study, however, it was found that the implementation burden of the PML, which requires substantial

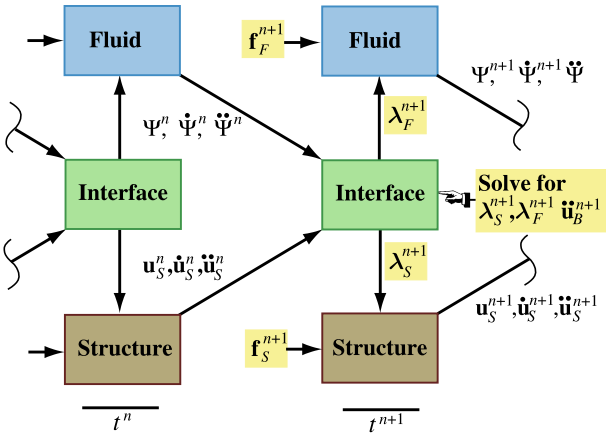

Fig. 7. Flowchart of the time-stepping procedure for LLM partitioned analysis.

tuning, would not be justified and that a simpler one would be sufficient. The simplest SB derivation technique makes use of the plane wave approximation (PWA), which follows directly from the Sommerfeld radiation condition. For a plane truncation boundary under an incident plane wave this condition, first introduced in acoustics by Mindlin and Bleich [28], reads

$$\frac{\partial p}{\partial n} = \frac{1}{c}\frac{\partial p}{\partial t} \quad \Rightarrow \quad p = \rho_{\mathrm{F}} c \dot{u}_n, \tag{28}$$

in which p is the pressure at the truncation boundary and $\dot{u}_n$ the normal fluid velocity there. The right side relation is the PWA [14]. The foregoing condition can be used to create a fluid damping matrix if the fluid equations are expressed in terms of the fluid displacement:

$$\mathbf{C}_{\mathrm{F}} = \int_{\Gamma_{\mathrm{F_{SB}}}} \rho_{\mathrm{F}} c \mathbf{N}^{\mathrm{T}} \mathbf{n}\mathbf{n}^{\mathrm{T}} \mathbf{N}\, \mathrm{d}\Gamma_{\mathrm{F_{SB}}}, \tag{29}$$

in which $\Gamma_{\mathrm{F_{SB}}}$ is the silent boundary, $\mathbf{n}$ the normal vector there, and $\mathbf{N}$ a standard linear shape function. To pass to the displacement potential as the fluid state variable, this fluid damping matrix is congruentially transformed by the gradient matrix ($\mathbf{D}_{\mathrm{F}}$) as previously done for the fluid stiffness and mass matrices, which yields $\mathbf{C}_{\mathrm{F}\psi} = \mathbf{D}_{\mathrm{F}}^{\mathrm{T}} \mathbf{C}_{\mathrm{F}} \mathbf{D}_{\mathrm{F}}$. The term multiplying $\delta\boldsymbol{\psi}$ in the total first variation of Π_{T} in (21) changes to $\delta\boldsymbol{\psi}^{\mathrm{T}}(\mathbf{M}_{\mathrm{F}\psi}\ddot{\boldsymbol{\psi}} + \mathbf{C}_{\mathrm{F}\psi}\dot{\boldsymbol{\psi}} + \mathbf{K}_{\mathrm{F}\psi}\boldsymbol{\psi} + \mathbf{D}_{\mathrm{F}}^{\mathrm{T}}\mathbf{B}_{\mathrm{F}n}\boldsymbol{\lambda}_{\mathrm{F}} - \mathbf{D}_{\mathrm{F}}^{\mathrm{T}}\mathbf{f}_{\mathrm{F}})$ and a damping submatrix $\mathbf{C}_{\mathrm{F}\psi}$ appears in the second term of (22). The fluid contributions in (25) change to

$$\begin{aligned} \mathbf{g}_{\mathrm{F}}^{n+1} &= \mathbf{D}_{\mathrm{F}}^{\mathrm{T}} \mathbf{f}_{\mathrm{F}}^{n+1} - \mathbf{C}_{\mathrm{F}\psi}[\dot{\mathbf{u}}_{\mathrm{F}}^{n} + \Delta t(1-\gamma)\ddot{\mathbf{u}}_{\mathrm{F}}^{n}] \\ &\quad - \mathbf{K}_{\mathrm{F}}\left[\mathbf{u}_{\mathrm{F}}^{n} + \Delta t\dot{\boldsymbol{\psi}}^{n} + \frac{\Delta t^2}{2}(1-2\beta)\ddot{\boldsymbol{\psi}}^{n}\right], \\ \widehat{\mathbf{K}}_{\mathrm{F}} &= \mathbf{M}_{\mathrm{F}\psi} + \Delta t\gamma\mathbf{C}_{\mathrm{F}\psi} + \Delta t^2\beta\mathbf{K}_{\mathrm{F}\psi}. \end{aligned} \tag{30}$$

With those changes the transient analysis can be performed as described in Section 6.

A silent boundary for the soil foundation, which is included in the structure partition, was constructed by the viscous damping boundary method (VDB) of [26]. The VDB is similar to the PWA in that it uses the idea

of adjoining viscous dampers to boundary element freedoms. However, for an elastic media such as soil one must take into account the presence of both primary (compressional) and secondary (shear) waves that travel through the media, and the appropriate wave speeds used instead of the speed of sound. Benchmark verification of the fluid SB accuracy and related modeling guidelines are discussed in [45].

8. Fluid cavitation

Inertial (also called transient) cavitation occurs in a liquid medium when the effective pressure (atmospheric plus hydrostatic plus dynamic) drops under a vaporization pressure threshold, leading to localized rupture and formation of tiny gas bubbles. The inception of this physical process is similar to boiling. A cavitating region may be macroscopically characterized as being roughly under a uniform gas–vapor pressure and bulk modulus near zero. The condition persists until the pressure is increased again by the collapse of the cavitated region [50], a rapid transient process that produces closure shocks. A simple but satisfactory macroscopic constitutive model is a bilinear one [3], in which the bulk modulus K is that of the liquid considered as an acoustic medium when the effective pressure is over the vaporization threshold, and zero otherwise. For simplicity, the threshold is often taken to be zero.

To incorporate this bilinear model, the effective pressure must be calculated at each time step over each element. Under the assumption of small liquid compressibility, the constitutive equation of Eq. (3) states that $p = -K\epsilon_V = -Ku_{\mathrm{F}i,i} = -\rho_{\mathrm{F}}c^2 u_{\mathrm{F}i,i}$. At a certain location in a fluid element e constructed with shape functions $\mathbf{N}_{\mathrm{F}}$, the dynamic pressure is determined by

$$p^e = -\rho_{\mathrm{F}}c^2\mathbf{B}_{vs}\mathbf{u}_{\mathrm{F}}^e, \tag{31}$$

where $\mathbf{u}_{\mathrm{F}}^e$ is extracted from the global displacements ($\mathbf{u}_{\mathrm{F}} = \mathbf{D}_{\mathrm{F}}\boldsymbol{\psi}$), and $\mathbf{B}_{vs}$ is the displacement-to-volumetric-strain matrix $\mathbf{B}_{vs} = \boldsymbol{\nabla}\mathbf{N}_{\mathrm{F}}$; cf. [10]. The effective pressure is then easily calculated by adding atmospheric and hydrostatic contributions.

This process can be implemented during the calculation of the stiffness matrix of the fluid. If reduced integration (one-point Gauss–Legendre rule) is used, only the pressure at the center of the element will be recovered by collocation. To obtain a smoother solution, the pressure is found at Gauss points for full integration (2×2 rule in 2D quadrilaterals or $2 \times 2 \times 2$ rule in 3D bricks). The element pressure is determined by interpolating to the center of the element and averaging, since recovered stresses are usually most accurate at locations within an element rather than on its boundaries [9].

When the effective pressure in the element drops below the vapor pressure, the stiffness matrix is modified to suppress rigidity for the element by setting $c = 0$. To reduce computational cost, the cavitation effect of each element on the matrix $\mathbf{K}_{\mathrm{F}\psi}$ is determined during the preprocessing phase, and that matrix adjusted accordingly. Furthermore, an explicit time integration scheme may be beneficial for two reasons. First, to accurately account for cavitation short time steps are needed to capture the high-frequency behavior, which makes an explicit scheme more attractive. Second, the computational cost is reduced since the dynamic fluid stiffness matrix, $\widehat{\mathbf{K}}_{\mathrm{F}\psi}$, lacks the contribution of $\mathbf{K}_{\mathrm{F}\psi}$, and may be reused for many steps as long as the timestep Δt is not changed.

Studies in the article series [30–32], show that the occurrence of cavitation can induce growing spurious pressure oscillations. These oscillations eventually cause fragmentation of the cavitation region, a phenomenon called *frothing*. The implementation for submarine hull cavitation [15] resolved this problem by the addition of an artificial damping term proportional to the apparent frequency. In the present study a Rayleigh damping matrix proportional to the fluid velocity was added to alleviate frothing and smooth out the solution:

$$\mathbf{C}_{\mathrm{F}d} = \alpha_K\mathbf{K}_{\mathrm{F}\psi} + \alpha_M\mathbf{M}_{\mathrm{F}\psi}. \tag{32}$$

The coefficients in (32) were adjusted to damp out high frequency frothing while preserving overall low frequency behavior.

9. Concept verification: infinite piston problem

A motion-driven, flexible-shaft piston compressing an infinite column of air is a benchmark problem that has been often used in computational aeroelasticity [4,11–13,27,41] to assess stability and accuracy of numerical simulations of gas dynamics coupled to a flexible structure. In this section, that problem is adjusted to capture features of target application problems [46]. The contained fluid is no longer a gas, but a liquid with parameters corresponding to water and terminated by a silent boundary (SB). The piston device is harmonically driven through a flexible shaft. Assuming 1D behavior, this problem has an exact analytical solution given below. This solution was used to verify the Mortar and LLM FSI interface treatments as well as the SB performance.

The problem is defined in Fig. 8, which also provides geometric and physical properties. Those are chosen to match roughly the properties of the gravity dam problem discussed in the sequel paper [46]. Here the spring stiffness is chosen to match the first natural frequency of the dam given a piston mass of 1.0 kg. The excitation frequency $\omega = 18$ rad/s is near the dominant frequency of the El Centro earthquake used in that problem.

9.1. Analytical solution

An analytical solution is possible by assuming that the fluid is acoustic, that its displacement $u_{\mathrm{F}} \equiv u$ is a function of x and t only, and that body forces are neglected. A PWA silent boundary expressed as $\dot{u}(L,t) = -cu'(L,t)$ is placed at a distance $x = L$, as shown in Fig. 8. Under those

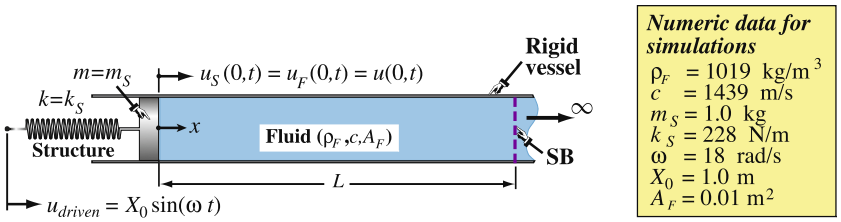

Fig. 8. Infinite piston benchmark problem.

assumptions, the fluid problem is governed by the bidirectional wave partial differential equation (PDE) [19]:

$$\frac{\partial^2 u}{\partial t^2} = c^2 \frac{\partial^2 u}{\partial x^2} \quad \text{or} \quad \ddot{u} = c^2 u'', \quad \text{in which } u = u(x,t), \quad x \geqslant 0,\ t > 0, \tag{33}$$

to be solved under the initial and boundary conditions

$$u(x,0) = 0, \quad \dot{u}(x,0) = 0, \quad \dot{u}(L,t) = -cu'(L,t), \tag{34}$$

$$m\ddot{u}(0,t) - \rho_F c^2 A_F u'(0,t) + ku(0,t) = kX_0 \sin(\omega t). \tag{35}$$

Of these (34) state the initial rest conditions and the SB at $x = L$, whereas (35) expresses the FSI equilibrium condition at the piston interface $x = 0$. The solution of (33)–(35) is worked out in [45] using the Laplace transform method. In transform space $t \to s$, $u \to U$ one gets

$$U(s,t) = \frac{k\omega X_0 \exp(-sx/c)}{(s^2+\omega^2)(k + \rho_F c A_F s + ms^2)}. \tag{36}$$

Back-transforming to physical space yields

$$u(x,t) = \frac{kX_0\omega}{d}\left\{a_1 a_2 + \frac{f_e}{\omega}\sin\left[\omega\left(t - \frac{x}{c}\right)\right] - f_d \cos\left[\omega\left(t - \frac{x}{c}\right)\right]\right\} H\left(t - \frac{x}{c}\right), \tag{37}$$

in which $f_d = \rho_F c A_F$, $f_e = k - m\omega^2$, $f_g = \sqrt{f_d^2 - 4km}$, $a_0 = \exp[(t - x/c)f_g/m]$, $a_1 = \exp[-((t - x/c)(f_d + f_g))/(2m)]/(2f_g)$, $a_2 = (a_0 - 1)(f_d^2 - 2f_e m) + (a_0 + 1)f_d f_g$, $d = f_e^2 + f_d^2\omega^2$, and H is the Heaviside unit step function. The piston displacement $u(0,t) = u_0(t)$ is obtained by taking $x = 0$. Note that the distance L to the SB has disappeared from (36) and (37). This shows that the PWA condition $\dot{u}(L,t) = -cu'(L,t)$, which precludes wave reflections, is exact for this model and could be applied at any L, including $L = 0$.

9.2. Matched mesh analysis verification

The benchmark problem is FEM-discretized in 3D by using a combination of solid and fluid bilinear brick elements with springs as illustrated in Fig. 9a. This figure shows an instance of matching fluid–structure meshes. The stiffness of the piston brick element is chosen sufficiently high so that the four springs control the structural flexibility. The excitation frequency is $\omega = 18$ rad/s. The analytical solution was verified first against the CASE spectral FSI code [47] and a pressure formulation discussed by Cook et al. [9]. These three models show excellent agreement as illustrated in Fig. 9b. The LLM interface treatment was then applied in conjunction with the Trapezoidal Rule (TR) version of Newmark and a timestep of 0.02 s. Excellent agreement is obtained as shown in Fig. 9c.

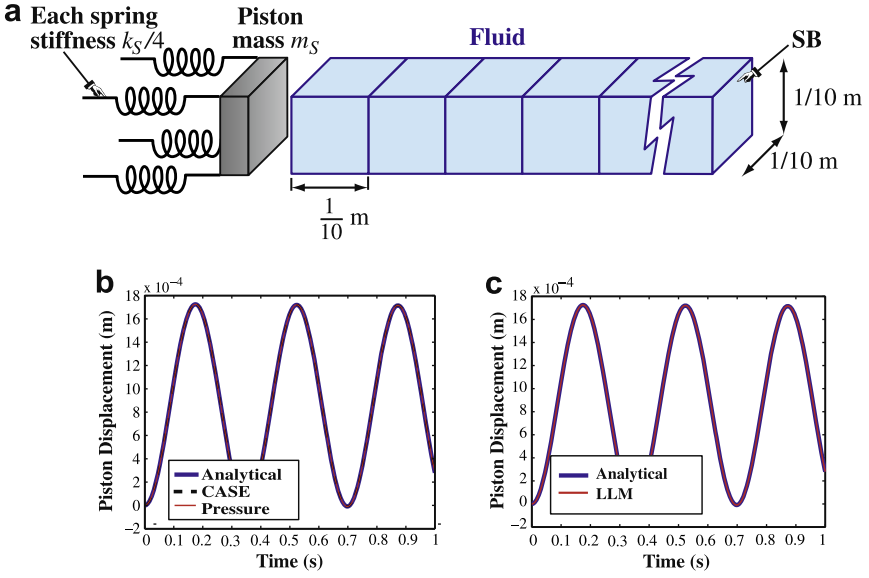

Fig. 9. Infinite piston problem with LLM-treated, matching-mesh interface.

9.3. Non-matching mesh analysis verification

Fig. 10a shows a 2×2 structure interface mesh linked to a 3×3 fluid interface mesh, where the fluid characteristic length, L_c, equals $\frac{1}{30}$m. Each fluid element is a cube with an edge length of L_c. Again the stiffness of the piston brick elements is chosen so high so that the five springs effectively govern the shaft flexibility. The excitation frequency is $\omega = 18$ rad/s. The TR was used for both fluid and structure with a timestep of $\Delta t = 0.01$ s. Response errors with respect to the analytical solution (37) at $x = 0$ were assessed with the C-error measure presented in [47].

The transient response for the model illustrated in Fig. 10a was carried out with two choices for the interface frame nodes: one based on the zero moment rule (ZMR, cf. Appendix B) as depicted in Fig. 10b, and one with frame nodes coincident with the fluid nodes. Both piston response histories showed no visible errors when plotted against the analytical solution. Fig. 11a shows the transient history for the second case. The C-errors were 0.0038 and 0.0083, respectively. In engineering calculations, C-errors less than 0.1 are typically considered satisfactory.

To further assess the performance of LLM for the non-matching case, the characteristic length L_c of the fluid mesh was systematically reduced, such that each fluid element remained a cube with an edge length of L_c while keeping the structure mesh fixed. Reduction of L_c increased the number of fluid interface nodes. The characteristic length, L_c, was varied from $\frac{1}{20}$m down to $\frac{1}{150}$m. Two interface frames were tested: (1) that produced by ZMR (this will be different for each L_c), and (2) one with nine frame nodes collocated at the structure nodes, a configuration labeled "matching coarse mesh."

C-error results for both interface frames are shown in Fig. 11b. Here we can observe an advantage of the ZMR: an interface discretized by the ZMR will converge faster.

10. Conclusions

We have presented the formulation of the primal-dual LLM method for treating the dynamic interaction between an acoustic fluid and a flexible structure. This treatment introduces additional interface variables, which include the frame kinematics and two multiplier sets. In a partitioned solution analysis procedure, those variables are algebraically solved separately at each time step, and multipliers are fed back into the fluid and structure equations. The increase in the number of variables and the implicit treatment of the interface equation is compensated by various advantages: (1) complete localization of fluid and structure models, (2) ability to handle non-matching

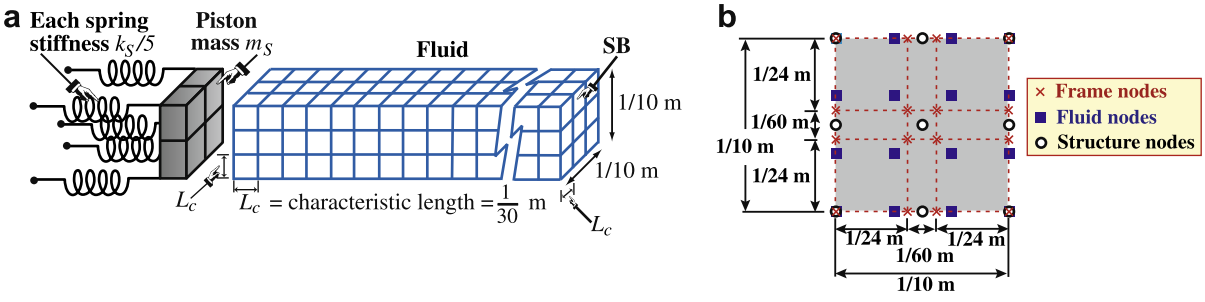

Fig. 10. Infinite piston problem with LLM-treated, non-matching mesh interface: (a) meshes for $L_c = \frac{1}{30}$ m, (b) ZMR for $L_c = \frac{1}{30}$ m.

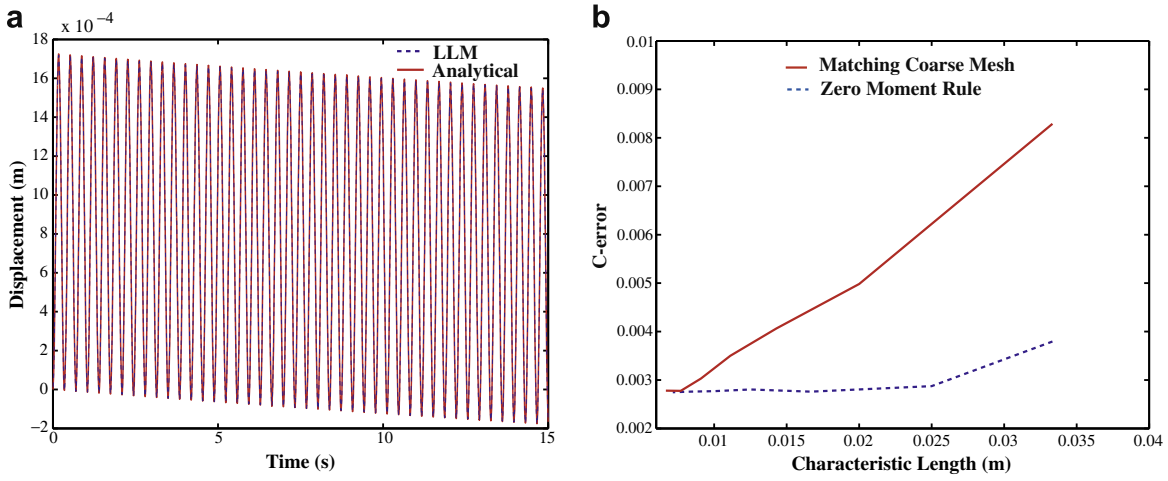

Fig. 11. Infinite piston response histories. (a) analytical versus LLM (frame nodes collocated at fluid nodes) piston displacements for $L_c = \frac{1}{30}$ m; (b) C-error for varying characteristic lengths, L_c.

meshes, and (3) retention of the stability and accuracy of the monolithic treatment. A welcome consequence of the first two advantages is additional freedom in making decisions at the modeling and solution stages, e.g., use of separate mesh generators, existing software for the separate partitions, and custom treatment of local nonlinearities.

A sequel paper [46] discusses the application and evaluation of this FSI method on a variety of problems that include a two-dimensional gravity dam and a three-dimensional arch dam, both under seismic action. In addition to transient response analysis the 2D dam problem includes vibration analysis and model reduction, while the 3D dam problem illustrates a mapping scheme to construct the LLM frame on doubly curved interfaces.

Acknowledgements

The research reported here was supported by the National Science Foundation under Grant High-Fidelity Simulations for Heterogeneous Civil and Mechanical Systems, CMS-0219422. The work of the first author was part of his doctoral dissertation while at the Department of Aerospace Engineering Sciences, University of Colorado at Boulder.

Appendix A. Stability and accuracy of mortar and LLM partitioned analysis

The following stability and accuracy analyses of partitioned analysis with Mortar and LLM interfacing treatments follow closely the spectral techniques of the paper that introduced FSI staggered solution methods [34]. The analysis relies on the construction of model systems that couple dry-vibration mode pairs of the structure and the fluid. In the following investigation, the fluid and structure semidiscrete equations are assumed to be expressed in terms of node displacement variables. Results for displacement-potential fluid variables are analogous and not included for brevity.

The analysis is first carried out for the Mortar method since the model equations are simpler. The conclusions are found to be directly applicable to the LLM method.

A.1. Mortar model system

The undamped, semidiscrete equations of motion of the FSI system linked by the Mortar method are

$$\begin{bmatrix} \mathbf{K}_\mathrm{S} & \mathbf{0} & \mathbf{B}_\mathrm{S} \\ \mathbf{0} & \mathbf{K}_\mathrm{F} & -\mathbf{B}_\mathrm{F} \\ \mathbf{B}_\mathrm{S}^\mathrm{T} & -\mathbf{B}_\mathrm{F}^\mathrm{T} & \mathbf{0} \end{bmatrix} \begin{Bmatrix} \mathbf{u}_\mathrm{S} \\ \mathbf{u}_\mathrm{F} \\ \boldsymbol{\lambda}_\mathrm{B} \end{Bmatrix} + \begin{bmatrix} \mathbf{M}_\mathrm{S} & \mathbf{0} & \mathbf{0} \\ \mathbf{0} & \mathbf{M}_\mathrm{F} & \mathbf{0} \\ \mathbf{0} & \mathbf{0} & \mathbf{0} \end{bmatrix} \begin{Bmatrix} \ddot{\mathbf{u}}_\mathrm{S} \\ \ddot{\mathbf{u}}_\mathrm{F} \\ \ddot{\boldsymbol{\lambda}}_\mathrm{B} \end{Bmatrix} = \begin{Bmatrix} \mathbf{f}_\mathrm{S} \\ \mathbf{f}_\mathrm{F} \\ \mathbf{0} \end{Bmatrix}. \tag{A.1}$$

This is the analog of (22), with only one set of connection matrices, and omitted gradient and damping matrices. The dimension of $\mathbf{u}_\mathrm{S}$, $\mathbf{u}_\mathrm{F}$ and $\boldsymbol{\lambda}_\mathrm{B}$ are n_S, n_F and n_λ, respectively. Matrices $\mathbf{K}_\mathrm{S}$ and $\mathbf{K}_\mathrm{F}$ are assumed to be symmetric and nonnegative, whereas $\mathbf{M}_\mathrm{S}$ and $\mathbf{M}_\mathrm{F}$ are symmetric and positive definite. The vibration eigenproblems associated with the *isolated* fluid and structure ($\boldsymbol{\lambda}_\mathrm{B} = \mathbf{0}$) are

$$\begin{aligned} &\mathbf{K}_\mathrm{S}\mathbf{v}_{\mathrm{S}i} = \omega_{\mathrm{S}i}^2 \mathbf{M}_\mathrm{S}\mathbf{v}_{\mathrm{S}i} \quad (i = 1, \ldots n_\mathrm{S}), \\ &\mathbf{K}_\mathrm{F}\mathbf{v}_{\mathrm{F}j} = \omega_{\mathrm{F}j}^2 \mathbf{M}_\mathrm{F}\mathbf{v}_{\mathrm{F}j} \quad (j = 1, \ldots n_\mathrm{F}). \end{aligned} \tag{A.2}$$

Here $\omega_{\mathrm{S}i}$ and $\omega_{\mathrm{F}j}$ are uncoupled vibration frequencies, whereas $\mathbf{v}_\mathrm{S}$ and $\mathbf{v}_\mathrm{F}$ are associated modes orthonormalized with respect to the respective mass matrices. Let matrices $\mathbf{V}_\mathrm{S}$ and $\mathbf{V}_\mathrm{F}$ be formed by collecting the $\mathbf{v}_{\mathrm{S}i}$ and $\mathbf{v}_{\mathrm{F}j}$ modes, respectively, as columns. Because of the chosen eigenvector orthonormalization, $\mathbf{V}_\mathrm{S}^\mathrm{T}\mathbf{M}_\mathrm{S}\mathbf{V}_\mathrm{S} = \mathbf{I}_\mathrm{S}$ and $\mathbf{V}_\mathrm{F}^\mathrm{T}\mathbf{M}_\mathrm{F}\mathbf{V}_\mathrm{F} = \mathbf{I}_\mathrm{F}$, in which $\mathbf{I}_\mathrm{S}$ and $\mathbf{I}_\mathrm{F}$ are the identity matrices of order n_S and n_F, respectively. The transformation equations to pass to normal coordinates are

$$\begin{aligned} \begin{Bmatrix} \mathbf{u}_\mathrm{S} \\ \mathbf{u}_\mathrm{F} \\ \boldsymbol{\lambda}_\mathrm{B} \end{Bmatrix} &= \begin{bmatrix} \mathbf{V}_\mathrm{S} & \mathbf{0} & \mathbf{0} \\ \mathbf{0} & \mathbf{V}_\mathrm{F} & \mathbf{0} \\ \mathbf{0} & \mathbf{0} & \boldsymbol{\Sigma} \end{bmatrix} \begin{Bmatrix} \mathbf{q}_\mathrm{S} \\ \mathbf{q}_\mathrm{F} \\ \mathbf{q}_\lambda \end{Bmatrix}, \\ \begin{Bmatrix} \ddot{\mathbf{u}}_\mathrm{S} \\ \ddot{\mathbf{u}}_\mathrm{F} \\ \ddot{\boldsymbol{\lambda}}_\mathrm{B} \end{Bmatrix} &= \begin{bmatrix} \mathbf{V}_\mathrm{S} & \mathbf{0} & \mathbf{0} \\ \mathbf{0} & \mathbf{V}_\mathrm{F} & \mathbf{0} \\ \mathbf{0} & \mathbf{0} & \boldsymbol{\Sigma} \end{bmatrix} \begin{Bmatrix} \ddot{\mathbf{q}}_\mathrm{S} \\ \ddot{\mathbf{q}}_\mathrm{F} \\ \ddot{\mathbf{q}}_\lambda \end{Bmatrix}, \end{aligned} \tag{A.3}$$

in which $\mathbf{q}_\mathrm{S}$, $\mathbf{q}_\mathrm{F}$ and $\mathbf{q}_\lambda$ are normal coordinates and where $\boldsymbol{\Sigma}$ is a $n_\lambda \times n_\lambda$ multiplier-scaling matrix. Applying (A.3) for a congruent transformation on (A.1) gives the normal system

$$\begin{bmatrix} \boldsymbol{\Omega}_\mathrm{S}^2 & \mathbf{0} & \mathbf{S} \\ \mathbf{0} & \boldsymbol{\Omega}_\mathrm{F}^2 & -\mathbf{F} \\ \mathbf{S}^\mathrm{T} & -\mathbf{F}^\mathrm{T} & \mathbf{0} \end{bmatrix} \begin{Bmatrix} \mathbf{q}_\mathrm{S} \\ \mathbf{q}_\mathrm{F} \\ \mathbf{q}_\lambda \end{Bmatrix} + \begin{bmatrix} \mathbf{I}_\mathrm{S} & \mathbf{0} & \mathbf{0} \\ \mathbf{0} & \mathbf{I}_\mathrm{F} & \mathbf{0} \\ \mathbf{0} & \mathbf{0} & \mathbf{0} \end{bmatrix} \begin{Bmatrix} \ddot{\mathbf{q}}_\mathrm{S} \\ \ddot{\mathbf{q}}_\mathrm{F} \\ \ddot{\mathbf{q}}_\lambda \end{Bmatrix} = \begin{Bmatrix} \mathbf{p}_\mathrm{S} \\ \mathbf{p}_\mathrm{F} \\ \mathbf{0} \end{Bmatrix} \tag{A.4}$$

in which $\boldsymbol{\Omega}_\mathrm{S}^2 = \mathbf{V}_\mathrm{S}^\mathrm{T}\mathbf{K}_\mathrm{S}\mathbf{V}_\mathrm{S} = \mathrm{diag}[\omega_{\mathrm{S}i}^2]$, $\boldsymbol{\Omega}_\mathrm{F}^2 = \mathbf{V}_\mathrm{F}^\mathrm{T}\mathbf{K}_\mathrm{F}\mathbf{V}_\mathrm{F} = \mathrm{diag}[\omega_{\mathrm{F}j}^2]$, $\mathbf{S} = \mathbf{V}_\mathrm{S}^\mathrm{T}\mathbf{B}_\mathrm{S}\boldsymbol{\Sigma}$, $\mathbf{F} = \mathbf{V}_\mathrm{F}^\mathrm{T}\mathbf{B}_\mathrm{F}\boldsymbol{\Sigma}$, $\mathbf{p}_\mathrm{S} = \mathbf{V}_\mathrm{S}^\mathrm{T}\mathbf{f}_\mathrm{S}$ and $\mathbf{p}_\mathrm{F} = \mathbf{V}_\mathrm{F}^\mathrm{T}\mathbf{f}_\mathrm{S}$. Although matrices $\boldsymbol{\Omega}_\mathrm{S}$, $\boldsymbol{\Omega}_\mathrm{F}$, $\mathbf{I}_\mathrm{S}$ and $\mathbf{I}_\mathrm{F}$ are diagonal, for a general $\boldsymbol{\Sigma}$ both $\mathbf{S}$ and $\mathbf{F}$ will be generally full, implying that each structural mode will generally be coupled to all fluid modes. Following behavioral assumptions similar to those of Appendix A of [34] the interaction of a mode pair, namely the ith structure mode and the jth fluid mode can be represented by the 3×3 model coupled system

$$\begin{bmatrix} \omega_{\mathrm{S}i}^2 & 0 & \varphi_{\mathrm{S}ij} \\ 0 & \omega_{\mathrm{F}j}^2 & -\varphi_{\mathrm{F}ij} \\ \varphi_{\mathrm{S}ij} & -\varphi_{\mathrm{F}ij} & 0 \end{bmatrix} \begin{Bmatrix} q_{\mathrm{S}i} \\ q_{\mathrm{F}j} \\ \lambda_{ij} \end{Bmatrix} + \begin{bmatrix} 1 & 0 & 0 \\ 0 & 1 & 0 \\ 0 & 0 & 0 \end{bmatrix} \begin{Bmatrix} \ddot{q}_{\mathrm{S}i} \\ \ddot{q}_{\mathrm{F}j} \\ \ddot{\lambda}_{ij} \end{Bmatrix} = \begin{Bmatrix} f_{\mathrm{S}i} \\ f_{\mathrm{F}j} \\ 0 \end{Bmatrix}. \tag{A.5}$$

Here $\varphi_{\mathrm{S}ij}$ and $\varphi_{\mathrm{F}ij}$ are scalars in the range 0 through 1 that characterize the strength of the interaction whereas λ_{ij} is a modal interaction multiplier obtained by appropriately choosing the ith and jth rows of $\boldsymbol{\Sigma}$. If $\varphi_{\mathrm{S}ij} = \varphi_{\mathrm{F}ij} = 0$ the modes do not interact and (A.5) uncouples into two scalar ODEs. It is therefore sufficient to investigate the time-

discretized stability and accuracy of the model system (A.5) for arbitrary but nonnegative frequencies $\omega_{Si} \geqslant 0$ and $\omega_{Fj} \geqslant 0$ as well as coupling factors $0 \leqslant \varphi_{Si} \leqslant 1$ and $0 \leqslant \varphi_{Fj} \leqslant 1$. This is done below for the Newmark time integration scheme.

A.2. Stability of mortar model system

To reduce clutter, modal indices i and j will be dropped. Forcing terms do not affect stability and are set to zero. Accordingly we consider the model system

$$\begin{bmatrix} \omega_S^2 & 0 & \varphi_S \\ 0 & \omega_F^2 & -\varphi_F \\ \varphi_S & -\varphi_F & 0 \end{bmatrix} \begin{bmatrix} q_S \\ q_F \\ \lambda \end{bmatrix} + \begin{bmatrix} 1 & 0 & 0 \\ 0 & 1 & 0 \\ 0 & 0 & 0 \end{bmatrix} \begin{Bmatrix} \ddot{q}_S \\ \ddot{q}_F \\ \ddot{\lambda} \end{Bmatrix} = \begin{Bmatrix} 0 \\ 0 \\ 0 \end{Bmatrix}. \tag{A.6}$$

This is not a conventional ODE, but a differential algebraic equation (DAE) of index 2 [5]. The computed values $q_S^k, q_F^k, \ldots$, where k is the step index, are assumed to satisfy exactly (A.6) except for roundoff, that is

$$\begin{aligned} &\omega_S^2 q_S^k + \varphi_S \lambda^k + \ddot{q}_S^k = 0, \quad \omega_F^2 q_S^k - \varphi_F \lambda^k + \ddot{q}_F^k = 0, \\ &\varphi_S q_S^k - \varphi_F q_F^k = 0, \end{aligned} \tag{A.7}$$

for $k = 0, 1, 2 \ldots$ In particular the initial conditions at $k = 0$ ($t = t_0 = 0$) are taken to satisfy (A.7) exactly. For further use introduce the state 6-vectors

$$\begin{aligned} \mathbf{z}^n &= [\, q_S^n \quad \dot{q}_S^n \quad \ddot{q}_S^n \quad q_F^n \quad \dot{q}_F^n \quad \ddot{q}_F^n \,]^{\mathrm{T}}, \\ \mathbf{z}^{n+1} &= [\, q_S^{n+1} \quad \dot{q}_S^{n+1} \quad \ddot{q}_S^{n+1} \quad q_F^{n+1} \quad \dot{q}_F^{n+1} \quad \ddot{q}_F^{n+1} \,]^{\mathrm{T}}. \end{aligned} \tag{A.8}$$

Computations have proceeded for n steps of constant stepsize $h = \Delta t$ up to $t^n = nh$. The Newmark formulas for displacements and velocities at the next time step $t^{n+1} = t^n + h$ are

$$\begin{aligned} q_S^{n+1} &= q_S^n + h\dot{q}_S^n + \frac{1}{2}h^2[2\beta\ddot{q}_S^{n+1} + (1-2\beta)\ddot{q}_S^n], \\ \dot{q}_S^{n+1} &= \dot{q}_S^n + h[\gamma\ddot{q}_S^{n+1} + (1-\gamma)\ddot{q}_S^n], \\ q_F^{n+1} &= q_F^n + h\dot{q}_F^n + \frac{1}{2}h^2[2\beta\ddot{q}_F^{n+1} + (1-2\beta)\ddot{q}_F^n], \\ \dot{q}_F^{n+1} &= \dot{q}_S^n + h[\gamma\ddot{q}_S^{n+1} + (1-\gamma)\ddot{q}_S^n], \end{aligned} \tag{A.9}$$

in which for simplicity the same parameters β and γ are selected for both fluid and structure. The following combinations of displacements, velocities and accelerations are used below:

$$\begin{aligned} \hat{q}_S^n &= q_S^n + h\dot{q}_S^n + \frac{1}{2}(1-\beta)h^2\ddot{q}_S^n, \\ \hat{q}_F^n &= q_F^n + h\dot{q}_F^n + \frac{1}{2}(1-\beta)h^2\ddot{q}_F^n, \\ \breve{q}_S^n &= h\dot{q}_S^n + (1-\gamma)h^2\ddot{q}_S^n, \\ \breve{q}_F^n &= h\dot{q}_F^n + (1-\gamma)h^2\ddot{q}_F^n. \end{aligned} \tag{A.10}$$

In the partitioned approach the interface force value λ^{n+1} is obtained from the model equations (A.7) evaluated at t^{n+1}, in conjunction with (A.9). The result can be compactly expressed as

$$\lambda^{n+1} = \frac{1}{\chi}[\, \varphi_S\chi_F \quad -\varphi_F\chi_S \,] \begin{bmatrix} \hat{q}_S^n \\ \hat{q}_F^n \end{bmatrix}, \tag{A.11}$$

in which $\chi_S = 1 + h^2\beta\omega_S^2$, $\chi_F = 1 + h^2\beta\omega_F^2$, $\chi = 2\beta h^2(\varphi_S^2\chi_F + \varphi_F^2\chi_S)$, and the last vector contains the combinations defined in (A.10). Substituting into (A.7) with $k = n+1$, along with (A.11), yields the next-step state values

$$\begin{Bmatrix} q_S^{n+1} \\ \dot{q}_S^{n+1} \\ \ddot{q}_S^{n+1} \\ q_F^{n+1} \\ \dot{q}_F^{n+1} \\ \ddot{q}_F^{n+1} \end{Bmatrix} = \frac{2}{\chi} \begin{bmatrix} h^2\beta\varphi_F^2 & h^2\beta\varphi_F\varphi_S \\ -h\gamma\kappa_S & h\gamma\varphi_F\varphi_S \\ -\kappa_S & \varphi_F\varphi_S \\ h^2\beta\varphi_F\varphi_S & h^2\beta\varphi_S^2 \\ h\gamma\varphi_F\varphi_S & -h\gamma\kappa_F \\ \varphi_F\varphi_S & -\kappa_F \end{bmatrix} \begin{Bmatrix} \hat{q}_S^n \\ \hat{q}_F^n \end{Bmatrix} + \begin{bmatrix} 0 & 0 \\ 1/h & 0 \\ 0 & 0 \\ 0 & 0 \\ 0 & 1/h \\ 0 & 0 \end{bmatrix} \begin{Bmatrix} \breve{q}_S^n \\ \breve{q}_F^n \end{Bmatrix}, \tag{A.12}$$

in which $\kappa_S = \varphi_S^2\chi_F + h^2\beta\varphi_F^2\omega_S^2$ and $\kappa_F = h^2\beta\varphi_S^2\omega_F^2 + \varphi_F^2\chi_S$. The coupling between fluid and structure variables in (A.12) is entirely due to the previous elimination of λ^{n+1}. From this equation it is easy to build, via entry-by-entry identification, the amplification relation

$$\mathbf{z}^{n+1} = \begin{Bmatrix} q_S^{n+1} \\ \dot{q}_S^{n+1} \\ \ddot{q}_S^{n+1} \\ q_F^{n+1} \\ \dot{q}_F^{n+1} \\ \ddot{q}_F^{n+1} \end{Bmatrix} = \begin{bmatrix} A_{11} & A_{12} & A_{13} & A_{14} & A_{15} & A_{16} \\ A_{21} & A_{22} & A_{23} & A_{24} & A_{25} & A_{26} \\ A_{31} & A_{32} & A_{33} & A_{34} & A_{35} & A_{36} \\ A_{41} & A_{42} & A_{43} & A_{44} & A_{45} & A_{46} \\ A_{51} & A_{52} & A_{53} & A_{54} & A_{55} & A_{56} \\ A_{61} & A_{62} & A_{63} & A_{64} & A_{65} & A_{66} \end{bmatrix} \times \begin{Bmatrix} q_S^n \\ \dot{q}_S^n \\ \ddot{q}_S^n \\ q_F^n \\ \dot{q}_F^n \\ \ddot{q}_F^n \end{Bmatrix} = \mathbf{A}\mathbf{z}^n. \tag{A.13}$$

Defining the FSI-coupled frequency

$$\tilde{\omega}^2 = \frac{\varphi_S^2\omega_F^2 + \varphi_F^2\omega_S^2}{\varphi_F^2 + \varphi_S^2}, \tag{A.14}$$

the characteristic polynomial of $\mathbf{A}$ can be presented in the compact form

$$P_A(\zeta) = \det(\mathbf{A} - \zeta\mathbf{I}) = \frac{\zeta^2\psi(2(\zeta-1)^2 + h^2\psi\tilde{\omega}^2)}{4\beta(1 + h^2\beta\tilde{\omega}^2)}, \tag{A.15}$$

in which $\psi = 1 + \zeta - 2\gamma(1-\zeta) + 2\beta(1-\zeta)^2$. The six characteristic roots ζ_i are the (generally complex) roots of

$P_A = 0$. Since $\beta > 0$, these will be the roots of the numerator. A-stability requires $|\zeta_i| \leqslant 1$ for any h and $\tilde{\omega}$. The two $\zeta = 0$ roots may be ignored and it is sufficient to examine the quartic polynomial $\psi(2(\zeta-1)^2 + h^2\psi\tilde{\omega}^2)$. Through the involutory transformation $\bar{\zeta} = (1+\zeta)/(1-\zeta)$, P_A is mapped to the Routh-Hurwitz polynomial

$$P_H = h^2\tilde{\omega}^2 + 16\hat{\gamma}h^2\tilde{\omega}^2\bar{\zeta} + 16(1 + (2\hat{\beta}+\hat{\gamma}^2)h^2\tilde{\omega}^2)\bar{\zeta}^2 + 32(\hat{\gamma} + 2\hat{\beta}\hat{\gamma}h^2\tilde{\omega}^2)\bar{\zeta}^3 + 64\hat{\beta}(1+\hat{\beta}h^2\tilde{\omega}^2)\bar{\zeta}^4 \qquad (A.16)$$

in which $\hat{\gamma} = \gamma - \frac{1}{2}$ and $\hat{\beta} = 2\beta - \gamma$. The Routh–Hurwitz stability conditions, omitting numeric coefficients, are $h^2\tilde{\omega}^2 \geqslant 0$, $\hat{\gamma}h^2\tilde{\omega}^2 \geqslant 0$, $h^2\hat{\gamma}\tilde{\omega}^2(1 + 2(\hat{\beta}+\hat{\gamma}^2)h^2\tilde{\omega}^2) \geqslant 0$, $h^2\hat{\gamma}^2\tilde{\omega}^2(1 + 2\hat{\gamma}^2h^2\tilde{\omega}^2(1+2\hat{\beta}h^2\tilde{\omega}^2)) \geqslant 0$ and $\hat{\beta}(1+h^2\hat{\beta}\tilde{\omega}^2) \geqslant 0$. By inspection these are met for any $\tilde{\omega}$ and h if and only if $\hat{\gamma}$ and $\hat{\beta}$ are nonnegative, or equivalently

$$2\beta \geqslant \gamma, \quad \gamma \geqslant \frac{1}{2}. \qquad (A.17)$$

These are the same A-stability conditions that hold for the Newmark method applied to a single oscillator with frequency $\tilde{\omega}$. In particular, the trapezoidal rule (TR) equivalent: $\beta = \frac{1}{4}$ and $\gamma = \frac{1}{2}$, satisfies (A.17).

A deeper spectral analysis of $P_A(\zeta)$ shows that the model coupled system (A.6) has three conjugate root pairs of different nature:

(1) A zero root pair associated with acceleration-only eigenvectors.
(2) A principal root pair dependent on h and $\tilde{\omega}$ that is identical to the principal pair of the Newmark method for a one-DOF oscillator. This pair is associated with the $\hat{q}$ modes of (A.10).
(3) A $\{h, \tilde{\omega}\}$-independent, parasitic root pair $(4\beta - 2\gamma - 1 \pm \sqrt{(1+2\gamma)^2 - 16\beta})/(4\beta)$, associated with the $\breve{q}$ modes of (A.10). These roots satisfy $|\zeta_i| \leqslant 1$ if (A.17) holds. For TR, the pair coalesces at $\zeta = -1$. If either of (A.17) is violated, one of these roots strays outside the unit circle, and the scheme is unstable for any h.

A.3. Accuracy of mortar model system

The exact solution of the DAE (A.6) is that of a free oscillator moving at the coupled frequency $\tilde{\omega}$ defined by (A.14). Assuming $\varphi_F \neq 0$ and initial conditions $q_S(0) = q_S^0$, $\dot{q}_S(0) = \dot{q}_S^0$, $q_F(0) = (\varphi_S/\varphi_F)q_S^0$ and $\dot{q}_F(0) = (\varphi_S/\varphi_F)\dot{q}_S^0$, the exact response is

$$q_S^{ex} = q_S^0\cos\tilde{\omega}t + \dot{q}_S^0\sin\tilde{\omega}t, \quad q_F^{ex} = \frac{\varphi_S}{\varphi_F}q_S^{ex},$$
$$\lambda^{ex} = \frac{\varphi_S(\omega_F^2 - \omega_S^2)}{\varphi_F^2 + \varphi_S^2}q_S^{ex}. \qquad (A.18)$$

To evaluate the local truncation error, take q_S^0 and $\dot{q}_S^0$ in (A.18) to be the computed values q_S^n and $\dot{q}_S^n$, respectively. Set $t = h$, subtract that solution from that delivered by $\mathbf{z}^{n+1} = \mathbf{A}\mathbf{z}^n$, and expand in h series at $t = t^n$, retaining the first nonzero term. Only the TR results $\left(\beta = \frac{1}{4}, \gamma = \frac{1}{2}\right)$ are displayed for brevity:

$$T_{q_S} = -\frac{1}{12}\dot{q}_S^n\tilde{\omega}^3h^3 + O(h^4), \quad T_{\dot{q}_S} = \frac{1}{12}q_S^n\tilde{\omega}^4h^3 + O(h^4),$$
$$T_{\ddot{q}_S} = \frac{1}{12}\dot{q}_S^n\tilde{\omega}^5h^3 + O(h^4), \quad T_{q_F} = -\frac{1}{12\varphi_F}\dot{q}_S^n\varphi_S\tilde{\omega}^3h^3 + O(h^4),$$
$$T_{\dot{q}_F} = \frac{1}{12\varphi_F}q_S^n\varphi_S\tilde{\omega}^4h^3 + O(h^4), \quad T_{\ddot{q}_F} = \frac{1}{12\varphi_F}\dot{q}_S^n\varphi_S\tilde{\omega}^5h^3 + O(h^4),$$
$$T_\lambda = \frac{1}{12(\varphi_F^2+\varphi_S^2)}\dot{q}_S^n\varphi_S\tilde{\omega}^3(\omega_S^2 - \omega_F^2)h^3 + O(h^4). \qquad (A.19)$$

This agrees with the accuracy of the TR-equivalent Newmark method applied to a single oscillator of frequency $\tilde{\omega}$. More generally, if $\gamma = \frac{1}{2}$ and $\beta \geqslant \frac{1}{4}$ all truncation errors in displacements, velocities, acceleration and interface forces are $O(h^3)$; consequently, the propagated (global) error is second order.

A.4. Stability and accuracy of LLM model system

The undamped, semidiscrete equations of motion of the FSI system linked by the LLM method to be investigated here are

$$\begin{bmatrix} \mathbf{K}_S & \mathbf{0} & \mathbf{B}_S & \mathbf{0} & \mathbf{0} \\ \mathbf{0} & \mathbf{K}_F & \mathbf{0} & \mathbf{B}_F & \mathbf{0} \\ \mathbf{B}_S^T & \mathbf{0} & \mathbf{0} & \mathbf{0} & -\mathbf{L}_{Sn} \\ \mathbf{0} & \mathbf{B}_F^T & \mathbf{0} & \mathbf{0} & -\mathbf{L}_{Fn} \\ \mathbf{0} & -\mathbf{L}_{Sn}^T & -\mathbf{L}_{Fn}^T & \mathbf{0} & \mathbf{0} \end{bmatrix} \begin{Bmatrix} \mathbf{u}_S \\ \mathbf{u}_F \\ \boldsymbol{\lambda}_S \\ \boldsymbol{\lambda}_F \\ \mathbf{u}_B \end{Bmatrix} + \begin{bmatrix} \mathbf{M}_S & \mathbf{0} & \mathbf{0} & \mathbf{0} & \mathbf{0} \\ \mathbf{0} & \mathbf{M}_F & \mathbf{0} & \mathbf{0} & \mathbf{0} \\ \mathbf{0} & \mathbf{0} & \mathbf{0} & \mathbf{0} & \mathbf{0} \\ \mathbf{0} & \mathbf{0} & \mathbf{0} & \mathbf{0} & \mathbf{0} \\ \mathbf{0} & \mathbf{0} & \mathbf{0} & \mathbf{0} & \mathbf{0} \end{bmatrix} \begin{Bmatrix} \ddot{\mathbf{u}}_S \\ \ddot{\mathbf{u}}_F \\ \ddot{\boldsymbol{\lambda}}_S \\ \ddot{\boldsymbol{\lambda}}_F \\ \ddot{\mathbf{u}}_B \end{Bmatrix} = \begin{Bmatrix} \mathbf{f}_S \\ \mathbf{f}_F \\ \mathbf{0} \\ \mathbf{0} \\ \mathbf{0} \end{Bmatrix}. \qquad (A.20)$$

This is a transcription of (22) that omits gradient and damping matrices. Following a spectral procedure similar to that discussed for the Mortar method, the following unforced model system is obtained:

$$\begin{bmatrix} \omega_S^2 & 0 & \varphi_S & 0 & 0 \\ 0 & \omega_F^2 & 0 & \varphi_F & 0 \\ \varphi_S & 0 & 0 & 0 & -\nu_S \\ 0 & \varphi_F & 0 & 0 & -\nu_F \\ 0 & 0 & -\nu_S & -\nu_F & 0 \end{bmatrix} \begin{Bmatrix} q_S \\ q_F \\ \lambda_S \\ \lambda_F \\ q_B \end{Bmatrix} + \begin{bmatrix} 1 & 0 & 0 & 0 & 0 \\ 0 & 1 & 0 & 0 & 0 \\ 0 & 0 & 0 & 0 & 0 \\ 0 & 0 & 0 & 0 & 0 \\ 0 & 0 & 0 & 0 & 0 \end{bmatrix} \begin{Bmatrix} \ddot{q}_S \\ \ddot{q}_F \\ \ddot{\lambda}_S \\ \ddot{\lambda}_F \\ \ddot{q}_B \end{Bmatrix} = \begin{bmatrix} 0 \\ 0 \\ 0 \\ 0 \\ 0 \end{bmatrix} \qquad (A.21)$$

in which the scalars φ_S, φ_F, ν_S and ν_F characterize the modal coupling strength. This is a DAE system of index 2, discretized at times $t^n = nh$ for $n = 0, 1, \ldots$, with q_S and q_F

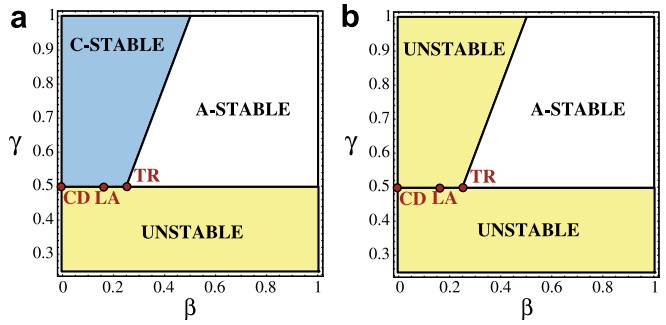

Fig. A.1. Summary of stability results for the Newmark integrator: (a) Monolithic solution; (b) Mortar and LLM partitioned solution with same (β,γ) used for fluid and structure. Labels TR, LA and CD mark the trapezoidal rule, linear acceleration and central difference instances, respectively.

treated by the Newmark integrator shown above. For further use define the FSI coupled frequency

$$\tilde{\omega}^2 = \frac{v_F^2\varphi_S^2\omega_F^2 + v_S^2\varphi_F^2\omega_S^2}{v_S^2\varphi_F^2 + v_F^2\varphi_S^2}. \tag{A.22}$$

Computations have proceeded until t^n. The interface values λ_S^{n+1}, λ_F^{n+1} and u_B^{n+1} are obtained by solving the model equation (A.22) evaluated at t^n, in conjunction with the Newmark formulas (A.9). The result is

$$\begin{bmatrix} \lambda_S^{n+1} \\ \lambda_F^{n+1} \\ \ddot{q}_B^{n+1} \end{bmatrix} = \frac{1}{\chi}\begin{bmatrix} v_F^2\varphi_S\chi_F & -v_Fv_S\varphi_F\chi_S \\ -v_Fv_S\varphi_S\chi_F & v_S^2\varphi_F\chi_S \\ \beta v_S\varphi_F^2\varphi_S & \beta v_F\varphi_F\varphi_S^2 \end{bmatrix}\begin{Bmatrix} \hat{q}_S^n \\ \hat{q}_F^n \end{Bmatrix}, \tag{A.23}$$

in which $\chi_S = 1 + h^2\beta\omega_S^2$, $\chi_F = 1 + h^2\beta\omega_F^2$, $\chi = \beta h^2(v_F^2\varphi_S^2\chi_F + v_S^2\varphi_F^2\chi_S)$, and the $\hat{q}$ displacements are defined in (A.10). Replacing into (A.21) at t^{n+1} provides the entries of $\mathbf{z}^{n+1}$ and the amplification matrix $\mathbf{A}$ relating $\mathbf{z}^{n+1} = \mathbf{A}\mathbf{z}^n$. This one is more complicated than (A.13), but its characteristic polynomial turns out to be

$$P_A(\zeta) = \det(\mathbf{A} - \zeta\mathbf{I}) = \frac{\zeta^2\psi(2(\zeta-1)^2 + h^2\psi\tilde{\omega}^2)}{4\beta(1 + h^2\beta\tilde{\omega}^2)}, \tag{A.24}$$

in which $\psi = 1 + \zeta - 2\gamma(1-\zeta) + 2\beta(1-\zeta)^2$. This polynomial is exactly that found for the Mortar method, except that $\tilde{\omega}$ is defined by (A.22) instead of (A.14). (They are identical if $v_S = v_F = 1$.) Consequently all conclusions reached for stability of the Mortar method hold without change for LLM. The accuracy analysis reveals that the truncation error is again $O(h^3)$ for $\gamma = \frac{1}{2}$; consequently, the propagated global error is second order.

Fig. A.1 summarizes our stability results on Mortar and LLM partitioned analysis with the Newmark time integrator. In that figure "C stable" means "conditionally stable"; that is, stable for a finite $h\omega$ range that includes $h = 0$.

Appendix B. The zero moment rule for placement of frame nodes

For non-matching meshes treated by LLM, the placement of frame nodes should obey conservation conditions that guarantee correct transmission of constant stress states across the interface. The set of those conditions is briefly referred to as the Interface Patch Test, or IPT. The problem was initially considered in the context of elastic contact [38,44]. In that application the frame materializes as bodies initially touch and is updated as a result of spreading contact and slip.

Suppose that it is desired to transmit a constant stress state $\boldsymbol{\sigma}_c$ across an interface Γ_B treated by LLM. The interface separates partitions labeled as $m = 1,\ldots,M$; usually $M = 2$. The preparatory steps listed in [38] are as follows.

(1) Select a layer of elements over each partition with nodes that contribute to the interface B.
(2) Given a typical element (e), obtain the strain-displacement relation $\mathbf{B}^e$. Evaluate at the element centroid of position $\mathbf{x}_c^e$ to get $\mathbf{B}_c^e = \mathbf{B}^e(\mathbf{x}_c^e)$.
(3) The contribution of the element to the interface node forces is $\mathbf{f}_c^e = V(\mathbf{B}_c^e)^{\mathrm{T}}\boldsymbol{\sigma}_c$, where V denotes the volume, area or length of the element depending on its dimensionality.
(4) Assemble the node interface forces in the usual manner over each partition to get $\mathbf{f}_c^m$, $m = 1,\ldots,M$. The interface multipliers are $\boldsymbol{\lambda}_c^m = -\mathbf{f}_c^m$. Collect all these in a vector $\mathbf{f}_c$.

Next assume that the frame Γ_B is FEM discretized by placing N_B nodes $\mathbf{x}_{Bi}$ on it, and appropriately choosing low-order conforming shape functions $\mathbf{N}_B$ over Γ_B. If the frame is one-dimensional (coupling two-dimensional elements), frame elements are line elements with piecewise linear shape functions. If the frame is two-dimensional (coupling three-dimensional elements), frame elements are triangles or quadrilaterals with piecewise linear or bilinear shape functions, respectively. The degrees of freedom of the frame are displacements collected in $\mathbf{u}_B$.

Consider an arbitrary virtual displacement $\delta\mathbf{u}_B$ of the frame. The points of application of the interface multiplier delta functions will move by amounts determined by the frame discretization. Collect those motions in $\delta\mathbf{u}_\lambda^m$ so that $\delta\Pi_{Bc} = \delta\mathbf{u}_B^{\mathrm{T}}\mathbf{f}_c$ is the virtual work spent on the boundary. Satisfaction of the IPT requires

$$\delta\Pi_{Bc} = 0, \tag{B.1}$$

for all admissible constant stress states $\boldsymbol{\sigma}_c$ and frame virtual displacements $\delta\mathbf{u}_B$. Meeting this requirement generally leads to a difficult inverse problem since the number and location of the frame nodes is not known in advance. An iterative process appears unavoidable. Fortunately, for a 1D frame that separates two 2D bodies, the problem can be solved directly using the Zero Moment Rule (ZMR) summarized below. Applying the ZMR in a tensor product form over 2D frame surfaces separating two 3D bodies often provides a good initial solution (or even the actual configuration if the frame surface has rectangular geometry, as illustrated in Fig. 10b for the infinite piston problem.)

The concept of the ZMR is best illustrated through an example. Consider the 2D fluid and structure non-matching

partitions pictured in Fig. B.1a. For this problem, the only stress of interest in the IPT is that normal to the interface AB. Points on the frame are mapped to the isoparametric coordinate ξ that ranges from $\xi = -1$ at A through $\xi = +1$ at B. The step-by-step process listed above produces the node forces shown as a consistent lumping from the normal-to-interface constant stress state. Only the numeric factors affecting those forces are given since that is sufficient to determine the frame node locations. This set satisfies translational and rotational self-equilibrium, as may be verified by inspection. The negated force set is applied to the frame viewed as an isolated object, as shown in Fig. B.1b. Consider now the frame as a Bernoulli-Euler beam, and compute the moment diagram $M(\xi)$, which is drawn in Fig. B.1c. The eight zero-moment points are candidates for frame node locations. Fig. B.1d shows possible frame configurations according to this rule. Of these, the latter would normally be chosen for a conventional dynamic analysis. Configurations with less nodes, which function like low-pass filters, may be of interest for model reduction and system identification studies [40]. Some extensions are discussed in [38].

The ZMR may be proven in various ways that range from physical arguments through purely mathematical manipulations. The following proof, based on that given in [39], is entirely algebraic and relies only on the principle of virtual work (PVW). It has the advantage of not asking where the interaction forces come from, and thus is extendible beyond FEM. Suppose the interface is a straight line segment that extends from $x = 0$ through $x = L$. For the ensuing manipulations it is convenient to *extend* the frame outside the interface proper so that its end points A, B are at $x_A = -a$ and $x_B = L + b$, where a and b are arbitrary positive values. The frame nodes are located at x_n, $n = 1, \ldots, N$ with $0 \leqslant x_n \leqslant L$. Also $x_{n+1} > x_n$, so no coincident nodes are allowed. Coordinates x_1 and x_N are taken as location of the first and last frame nodes, respectively, a decision subject to *a posteriori* verification. For brevity call the transverse displacement of the frame $w(x)$, which is taken to be C^0 continuous and piecewise-linear between frame nodes. This is conventionally prolonged with constant values to cover the remainder of the frame, so that $w(x) = w(x_1)$ for $x_A \leqslant x \leqslant x_1$, and $w(x) = w(x_N)$ for $x_N \leqslant x \leqslant x_B$. The PVW test function is δw.

Call $V = V_A + \int_A^x q(x)\mathrm{d}x$ and $M(x) = M_A + \int_0^x V(x)\mathrm{d}x$ so that $q = \mathrm{d}^2M/\mathrm{d}x^2 = M''$, where $(\cdot)\prime \equiv \mathrm{d}(\cdot)/\mathrm{d}x$. From those definitions $V(x)$ and $M(x)$ are the transverse shear and bending moment functions, respectively, associated with the force system $q(x)$.

The frame virtual work is $\delta W = \int_A^B q(x)\delta w(x)\mathrm{d}x$. Setting δw to be a linear function in $x \in [0, L]$ requires the applied forces to satisfy global translational and rotational equilibrium, but places no conditions on frame node locations. To do that δW is integrated twice by parts:

$$\delta W = M_A\delta w'_A - M_B\delta w'_B + V_B\delta w_B - V_A\delta w_A + \int_A^B M(x)w''\mathrm{d}x. \tag{B.2}$$

However, $\delta w'_A = \delta w'_B = 0$ since $w(x)$ is constant there. Next, take $\delta w_A = \delta w_1 = 1$, $\delta w_B = \delta w_N = 0$, and interpolate linearly between w_1 and w_N; then $\delta W = V_A = 0$ because there are no forces between x_A and $x_1 = 0$. Likewise take $\delta w_A = \delta w_1 = 0$, $\delta w_B = \delta w_N = 1$, and a linear interpolation between w_1 and w_N; then $\delta W = V_B = 0$ because there are no forces between $x_N = L$ and x_B. Consequently all boundary terms in (B.2) vanish. Since $w(x)$ is piecewise linear between frame nodes so is $\delta w(x)$. At a frame node n the following weighted-finite-difference relation holds:

$$\delta w''_n = \frac{\delta w_{n+1} - \delta w_n}{\Delta x_n^+} - \frac{\delta w_n - \delta w_{n-1}}{\Delta x_n^-}, \tag{B.3}$$

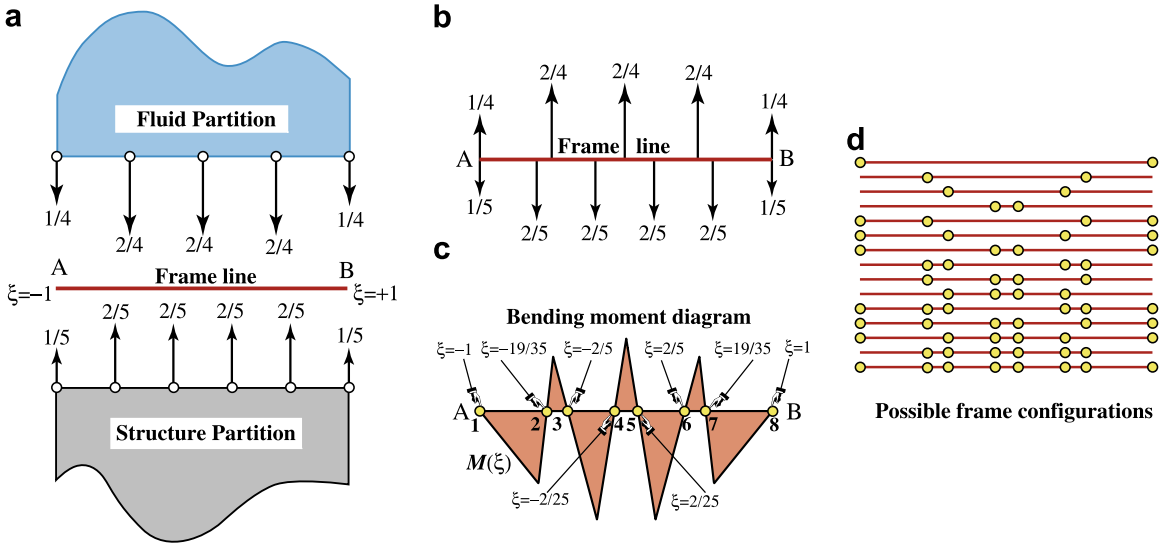

Fig. B.1. Zero moment rule: an example.

where $\Delta x_n^+ = x_{n+1} - x_n > 0$ and $\Delta x_n^- = x_n - x_{n-1} > 0$. For the first node ($n = 1$), $x_{n-1} = x_0$ is conventionally taken to be at A; for the last node ($n = N$), x_{n+1} is taken to be at B. At location other than nodes, $\delta w'' = 0$. Hence

$$\delta W = \sum_n M(x_n)\delta w''(n) = \sum_n M(x_n)\left(\frac{\delta w_{n+1} - \delta w_n}{\Delta x_n^+} - \frac{\delta w_n - \delta w_{n-1}}{\Delta x_n^-}\right) = 0. \quad \text{(B.4)}$$

At nodes $n = 2, \ldots, N-1$ take $\delta w_{n+1} = \delta w_{n-1} = 0$, $\delta w_n = 1$; since $\Delta x_n^+ > 0$ and $\Delta x_n^- > 0$, (B.4) requires $M(x_n) = 0$. At node 1 take $\delta w_A = \delta w_1 = 1$ and $\delta w_2 = 0$, which requires $M(x_1) = 0$. At node N take $\delta w_N = \delta w_B = 1$ and $\delta w_{N-1} = 0$, which requires $M(x_N) = 0$. Therefore $M(x)$ must vanish at all frame nodes. We note that $M(x_1) = M(x_N) = 0$ because there are no forces to the left of $x = x_1$ and to the right of $x = x_N$, thus justifying the *a priori* choice of those locations as first and last frame nodes, respectively. Consequently the one-dimensional ZMR is proved.

Appendix C. FSI modeling example: finite piston

This Appendix gives a 1D tutorial example intended for readers unfamiliar with (1) multiplier-based FSI treatment and (2) displacement potential variables. To help with (1), three interface treatments are shown: monolithic, Mortar and LLM. To help with (2) the transformation from fluid node displacements to displacement potential freedoms is worked out in detail. Unlike the verification problem of Section 9, the piston is finite so that no SB intrudes as a complicating factor. The discretization is sufficiently coarse so that all matrix equations can be explicitly displayed.

The problem is illustrated in Fig. C.1a. A cylinder of acoustic fluid enclosed in a rigid vessel is compressed by a rigid piston restrained by an elastic spring. All of the structural mass m_S is lumped at the piston. The system is excited by a time-harmonic force $P = P_0 e^{j\omega_p t}$ applied on the piston, where P_0 are ω_p are the driving amplitude and frequency, respectively. Geometric and physical properties are given in the figure. The only characteristic length of the problem is the enclosed cylinder length L.

The structure and the fluid are discretized as shown in Fig. C.1b. The structure may be discretized with a single bar element. For the fluid, two elements is the minimum discretization when the displacement potential ψ is picked as the primary variable. After establishing the basic relations the dynamic equations of motion will be set up with monolithic, LLM and Mortar treatments with two choices of primary variables for the fluid. The dynamic piston impedance will be compared between these combinations.

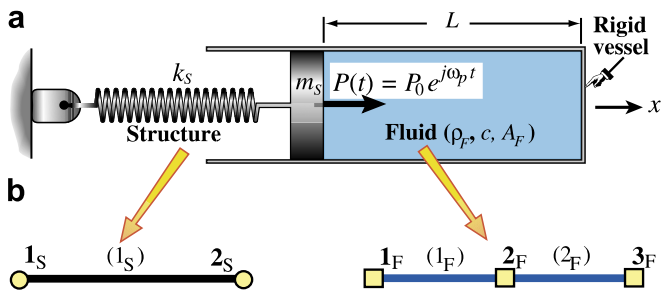

Fig. C.1. Finite element model of finite piston problem.

C.1. Fluid displacement formulation

For convenience, define $k_F = \rho_F c^2 A_F / L$ as equivalent fluid stiffness and $m_F = \rho_F A_F L$ as total fluid mass, respectively. Then, the structural and fluid mass and stiffness matrices in terms of freedoms $\{u_{S1}, u_{S2}\}$ and $\{u_{F1}, u_{F2}, u_{F2}\}$ are given by

$$\mathbf{K}_S = k_S \begin{bmatrix} 1 & -1 \\ -1 & 1 \end{bmatrix}, \quad \mathbf{K}_F = 2k_F \begin{bmatrix} 1 & -1 & 0 \\ -1 & 2 & -1 \\ 0 & -1 & 1 \end{bmatrix},$$

$$\mathbf{M}_S = m_S \begin{bmatrix} 0 & 0 \\ 0 & 1 \end{bmatrix}, \quad \mathbf{M}_F = (1-\mu)\mathbf{M}_{FC} + \mu \mathbf{M}_{FL},$$

$$\mathbf{M}_{FC} = \frac{m_F}{12} \begin{bmatrix} 2 & 1 & 0 \\ 1 & 4 & 1 \\ 0 & 1 & 2 \end{bmatrix}, \quad \mathbf{M}_{FL} = \frac{m_F}{4} \begin{bmatrix} 1 & 0 & 0 \\ 0 & 2 & 0 \\ 0 & 0 & 1 \end{bmatrix}, \quad \text{(C.1)}$$

in which the fluid mass matrix has been expressed as a linear combination of the consistent and lumped mass matrices $\mathbf{M}_{FC}$ and $\mathbf{M}_{FL}$. The optimal mass matrix is known to be given by $\mu = 1/2$ [18].

The monolithic treatment of the interaction is displayed in Fig. C.2(a). Here $u_{S2} = u_{F1} = u_2$. Using (C.1) with $\mu = 1/2$ and applying the fixed end conditions $u_{S1} = u_{F3} = 0$ gives the equations of motion

$$\begin{bmatrix} k_S + 2k_F & -2k_F \\ -2k_F & 4k_F \end{bmatrix} \begin{bmatrix} u_2 \\ u_3 \end{bmatrix} + \begin{bmatrix} m_S + \frac{5}{24}m_F & \frac{1}{24}m_F \\ \frac{1}{24}m_F & \frac{10}{24}m_F \end{bmatrix} \begin{bmatrix} \ddot{u}_2 \\ \ddot{u}_3 \end{bmatrix} = \mathbf{f}_T = \begin{bmatrix} P_0 e^{j\omega_p t} \\ 0 \end{bmatrix}. \quad \text{(C.2)}$$

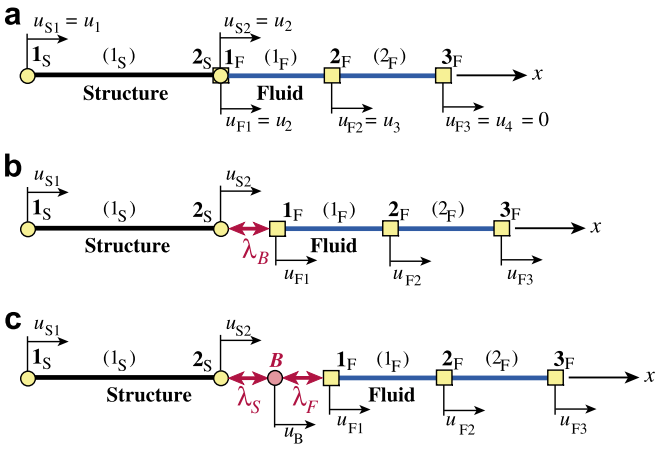

Fig. C.2. Fluid displacement models of a finite piston problem: (a) monolithic formulation; (b) Mortar (aka global Lagrange multiplier) formulation; (c) localized Lagrange multiplier (LLM) formulation.

It is convenient to reduce these to dimensionless form. To do that we introduce the following definitions, originally used in [34]:

$$\xi = \frac{m_S}{m_F}, \quad \Phi^2 = \frac{k_S L^2}{\xi m_S c^2}, \quad \tau = \frac{ct}{L}, \quad \dot{(\cdot)} \equiv \frac{\mathrm{d}(\cdot)}{\mathrm{d}\tau}, \\ \mu = u/L, \quad \Omega = \frac{\omega L}{c}, \quad \Omega_p = \frac{\omega_p L}{c}, \quad \phi_0 = \frac{P_0}{k_F L}. \tag{C.3}$$

Here ξ is a structure-to-fluid mass ratio, Φ is a ratio of in-vacuo structural frequency to acoustic frequency scaled by $1/\sqrt{\xi}$, τ is a reduced or dimensionless time ($\tau = 1$ is the time needed by a fluid sound wave to travel the characteristic length L), μ is a displacement normalized to L, Ω and Ω_P are dimensionless frequencies, and ϕ_0 is a scaled piston force amplitude. A darker dot denotes derivative respect to τ. All stiffness–mass ratios are collected in the following table:

	num			
den	k_S	k_F	m_S	m_F
k_S	1	$1/(\xi^2\Phi^2)$	$L^2/(\xi c^2\Phi^2)$	$L^2/(\xi^2 c^2\Phi^2)$
k_F	$\xi^2\Phi^2$	1	$\xi L^2/c^2$	L^2/c^2
m_S	$\xi c^2\Phi^2/L^2$	$c^2/(\xi L^2)$	1	$1/\xi$
m_F	$\xi^2 c^2\Phi^2/L^2$	c^2/L^2	ξ	1

On dividing (C.2) by $m_F L$ and using (C.3) as well as the foregoing table the equations of motion are put in dimensionless form

$$\begin{bmatrix} \xi^2\Phi^2 + 2 & -2 \\ -2 & 4 \end{bmatrix} \begin{bmatrix} \mu_1 \\ \mu_2 \end{bmatrix} + \begin{bmatrix} \xi + \frac{5}{24} & \frac{1}{24} \\ \frac{1}{24} & \frac{10}{24} \end{bmatrix} \begin{bmatrix} \ddot{\mu}_1 \\ \ddot{\mu}_2 \end{bmatrix} = \begin{bmatrix} \phi_0 \mathrm{e}^{\mathrm{j}\Omega_p \tau} \\ 0 \end{bmatrix}. \tag{C.4}$$

Assuming a periodic motion $\mu_i = \hat{\mu}_i \mathrm{e}^{\mathrm{j}\Omega\tau}$ for the unforced system we obtain the characteristic equation

$$\det\left(\begin{bmatrix} \xi^2\Phi^2 + 2 & -2 \\ -2 & 4 \end{bmatrix} - \Omega^2 \begin{bmatrix} \xi + \frac{5}{24} & \frac{1}{24} \\ \frac{1}{24} & \frac{10}{24} \end{bmatrix} \right) = 0, \tag{C.5}$$

which gives two dimensionless natural frequencies

$$\frac{\Omega_1^2}{\Omega_2^2} = \frac{24(22 + 48\xi + 5\xi^2\Phi^2 \mp \sqrt{288 + 1152\xi - 480\xi^3\Phi^2 + 25\xi^4\Phi^4 + 24\xi^2(96 + \Phi^2)})}{49 + 240\xi}, \tag{C.6}$$

and the piston admittance

$$G_{11} = \frac{48(5\Omega^2 - 48)}{48(5\Omega^2 - 48)\xi(\xi\Phi^2 - \Omega^2) + 1056\Omega^2 - 49\Omega^4 - 2304}. \tag{C.7}$$

This has poles at $\Omega = \Omega_1$ and $\Omega = \Omega_2$. Results (C.6) and (C.7) are taken as reference for subsequent comparisons.

Mortar treatment. The interaction treatment by Mortar is schematized in Fig. C.2b. On adjoining multiplier λ_B the equations of motion become

$$\begin{bmatrix} \xi^2\Phi^2 & 0 & 0 & 1 \\ 0 & 2 & -2 & -1 \\ 0 & -2 & 4 & 0 \\ 1 & -1 & 0 & 0 \end{bmatrix} \begin{bmatrix} \mu_{S2} \\ \mu_{F1} \\ \mu_{F2} \\ \lambda_B \end{bmatrix} + \begin{bmatrix} \xi & 0 & 0 & 0 \\ 0 & \frac{5}{24} & \frac{1}{24} & 0 \\ 0 & \frac{1}{24} & \frac{5}{12} & 0 \\ 0 & 0 & 0 & 0 \end{bmatrix} \begin{bmatrix} \ddot{\mu}_{S2} \\ \ddot{\mu}_{F1} \\ \ddot{\mu}_{F2} \\ \ddot{\lambda}_B \end{bmatrix} = \begin{bmatrix} \phi_S \mathrm{e}^{\mathrm{j}\Omega_p \tau} \\ 0 \\ 0 \\ 0 \end{bmatrix}. \tag{C.8}$$

In compact matrix form: $\mathbf{K}_G \mathbf{u}_G + \mathbf{M}_G \ddot{u}_G = \mathbf{f}_G$. It may be verified that the characteristic equation $\det(\mathbf{K}_G - \Omega^2 \mathbf{M}_G) = 0$ is quadratic in Ω^2. It yields the same natural frequencies as (C.6). The piston admittance is identical to (C.7).

LLM treatment. The interaction treatment by LLM is schematized in Fig. C.2c. On adjoining a frame (actually just one point in this problem) with axial displacement u_B and two Lagrange multipliers λ_F and λ_F that connect the frame to the structure and fluid, respectively, the equations of motion become

$$\begin{bmatrix} \xi^2\Phi^2 & 0 & 0 & -1 & 0 & 0 \\ 0 & 2 & -2 & 0 & -1 & 0 \\ 0 & -2 & 4 & 0 & 0 & 0 \\ -1 & 0 & 0 & 0 & 0 & 1 \\ 0 & -1 & 0 & 0 & 0 & 1 \\ 0 & 0 & 0 & 1 & 1 & 0 \end{bmatrix} \begin{bmatrix} \mu_{S2} \\ \mu_{F1} \\ \mu_{F2} \\ \lambda_S \\ \lambda_F \\ \mu_B \end{bmatrix} \\ + \begin{bmatrix} \xi & 0 & 0 & 0 & 0 & 0 \\ 0 & \frac{5}{24} & \frac{1}{24} & 0 & 0 & 0 \\ 0 & \frac{1}{24} & \frac{5}{12} & 0 & 0 & 0 \\ 0 & 0 & 0 & 0 & 0 & 0 \\ 0 & 0 & 0 & 0 & 0 & 0 \\ 0 & 0 & 0 & 0 & 0 & 0 \end{bmatrix} \begin{bmatrix} \ddot{\mu}_{S2} \\ \ddot{\mu}_{F1} \\ \ddot{\mu}_{F2} \\ \ddot{\lambda}_S \\ \ddot{\lambda}_F \\ \ddot{\mu}_B \end{bmatrix} = \begin{bmatrix} \phi_0 \mathrm{e}^{\mathrm{j}\Omega_p \tau} \\ 0 \\ 0 \\ 0 \\ 0 \\ 0 \end{bmatrix}. \tag{C.9}$$

In compact matrix form: $\mathbf{K}_L \mathbf{u}_L + \mathbf{M}_L \ddot{u}_L = \mathbf{f}_L$. It may be verified that the characteristic equation $\det(\mathbf{K}_L - \Omega^2 \mathbf{M}_L) = 0$ is quadratic in Ω^2 and yields the same natural frequencies as (C.6). The piston admittance is identical to (C.7).

C.2. Displacement potential formulation

Next, a dimensionless version of the displacement potential $\psi(x)$ is adopted as the fluid primary variable. The definition is

$$\mu(x) = \frac{u(x)}{L} = \frac{\mathrm{d}\psi(x)}{\mathrm{d}x} = \psi'. \tag{C.10}$$

For pointwise correspondence with piecewise linear displacement elements one would need 3-node, piecewise-qua-

dratic displacement potential elements. However in the present context only piecewise-linear 2-node elements in ψ will be considered. This decision in turn suggests adding a fictitious element and a fictitious node outside the piston, as pictured in Fig. C.3. The fluid nodal freedoms are ψ_1 through ψ_4. If the fictitious element and node are omitted, previous results are not recovered because the model becomes kinematically overconstrained: no fluid DOFs remain.

The finite difference gradient matrix to pass from fluid displacements to displacement potential freedoms is

$$\begin{bmatrix} u_{F1} \\ u_{F2} \\ u_{F3} \end{bmatrix} = \frac{1}{L}\begin{bmatrix} -2 & 2 & 0 & 0 \\ -1 & 0 & 1 & 0 \\ 0 & -1 & 0 & 1 \end{bmatrix}\begin{bmatrix} \psi_1 \\ \psi_2 \\ \psi_3 \\ \psi_4 \end{bmatrix}. \tag{C.11}$$

The boundary condition $u_{F3} = 0$ is enforced (as an essential condition) by setting $\psi_4 = \psi_2$. Furthermore, one of the ψ_i values may be set to an arbitrary constant, say zero. We chose $\psi_3 = 0$, whence the transformation contracts to

$$\begin{bmatrix} u_{F1} \\ u_{F2} \end{bmatrix} = \frac{1}{L}\begin{bmatrix} -2 & 2 \\ -1 & 0 \end{bmatrix}\begin{bmatrix} \psi_1 \\ \psi_2 \end{bmatrix} = \mathbf{D}_F\boldsymbol{\psi}. \tag{C.12}$$

Note that applying this transformation to the monolithic treatment makes no sense since u_{F1} and u_{S2} coalesce. Therefore we consider below only the multiplier-coupled systems.

Mortar treatment. The Mortar interface coupling is pictured in Fig. C.4a. Applying the congruential transformation gives the fluid stiffness and mass in terms of displacement potentials, whence the equations of motion become

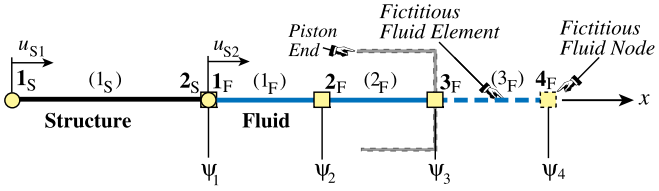

Fig. C.3. Displacement potential formulation of piston problem. Additional (fictitious) fluid element and node are appended to permit correlation to results from the displacement treatment.

$$\begin{bmatrix} \xi^2\Phi^2 & 0 & 0 & 1 \\ 0 & 4 & -4 & 2 \\ 0 & -4 & 8 & -2 \\ 1 & 2 & -2 & 0 \end{bmatrix}\begin{bmatrix} \mu_{S2} \\ \psi_{F1} \\ \psi_{F2} \\ \lambda_B \end{bmatrix} + \begin{bmatrix} \xi & 0 & 0 & 0 \\ 0 & \frac{17}{12} & -\frac{11}{12} & 0 \\ 0 & -\frac{11}{12} & \frac{5}{6} & 0 \\ 0 & 0 & 0 & 0 \end{bmatrix}\begin{bmatrix} \ddot{\mu}_{S2} \\ \ddot{\psi}_{F1} \\ \ddot{\psi}_{F2} \\ \ddot{\lambda}_B \end{bmatrix} = \begin{bmatrix} \phi_0 e^{j\Omega_p \tau} \\ 0 \\ 0 \\ 0 \end{bmatrix}. \tag{C.13}$$

Multiplier λ_B couples now to two fluid nodes 1_F and 2_F, so the picture in Fig. C.4(a) is somewhat idealized. In compact matrix form: $\mathbf{K}_G^{\psi}\mathbf{u}_L + \mathbf{M}_G^{\psi}\ddot{u}_G^{\psi} = \mathbf{f}_G^{\psi}$. It may be verified that the characteristic equation $\det(\mathbf{K}_G^{\psi} - \Omega^2\mathbf{M}_G^{\psi}) = 0$ is quadratic in Ω^2 and yields the same natural frequencies as (C.6). The piston admittance is identical to (C.7).

LLM treatment. The LLM interface coupling is shown in Fig. C.4b. Applying the congruential transformation gives the fluid stiffness and mass in terms of displacement potentials, whence the equations of motion become

$$\begin{bmatrix} \xi^2\Phi^2 & 0 & 0 & -1 & 0 & 0 \\ 0 & 4 & -4 & 0 & 2 & 0 \\ 0 & -4 & 8 & 0 & -2 & 0 \\ -1 & 0 & 0 & 0 & 0 & 1 \\ 0 & 2 & -2 & 0 & 0 & 1 \\ 0 & 0 & 0 & 1 & 1 & 0 \end{bmatrix}\begin{Bmatrix} \mu_{S2} \\ \psi_{F1} \\ \psi_{F2} \\ \lambda_S \\ \lambda_F \\ \mu_B \end{Bmatrix} + \begin{bmatrix} \xi & 0 & 0 & 0 & 0 & 0 \\ 0 & \frac{17}{12} & -\frac{11}{12} & 0 & 0 & 0 \\ 0 & -\frac{11}{12} & \frac{5}{6} & 0 & 0 & 0 \\ 0 & 0 & 0 & 0 & 0 & 0 \\ 0 & 0 & 0 & 0 & 0 & 0 \\ 0 & 0 & 0 & 0 & 0 & 0 \end{bmatrix}\begin{bmatrix} \ddot{\mu}_{S2} \\ \ddot{\psi}_{F1} \\ \ddot{\psi}_{F2} \\ \ddot{\lambda}_S \\ \ddot{\lambda}_F \\ \ddot{\mu}_B \end{bmatrix} = \begin{Bmatrix} \phi_0 e^{j\Omega_p \tau} \\ 0 \\ 0 \\ 0 \\ 0 \\ 0 \end{Bmatrix}. \tag{C.14}$$

Multiplier λ_F couples now to two fluid nodes 1_F and 2_F, so the picture in Fig. C.4(b) is somewhat idealized. In compact matrix form: $\mathbf{K}_L^{\psi}\mathbf{u}_L + \mathbf{M}_L^{\psi}\ddot{u}_G^{\psi} = \mathbf{f}_L^{\psi}$. It may be verified that the characteristic equation $\det(\mathbf{K}_L^{\psi} - \Omega^2\mathbf{M}_L^{\psi}) = 0$ is quadratic in Ω^2 and yields the same natural frequencies as (C.6). The piston admittance is identical to (C.7).

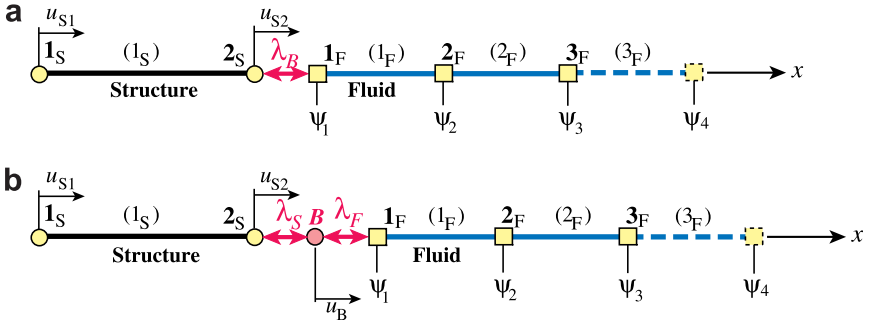

Fig. C.4. Displacement potential formulation of piston problem. Additional (fictitious) fluid element and node are appended to permit correlation to results from the displacement treatment.

References

[1] J.P. Berenger, A perfectly matched layer for the absorption of electromagnetic waves, J. Comput. Phys. 114 (1990) 185–200.

[2] C. Bernardi, Y. Maday, A.T. Patera, A new nonconforming approach to domain decomposition: the mortar element method. Technical Report, Université Pierre at Marie Curie, Paris, France, 1990.

[3] H.H. Bleich, I.S. Sandler, Interaction between structures and bilinear fluids, Int. J. Solids Struct. 6 (1970) 617–639.

[4] F. Blom, A monolithical fluid–structure interaction algorithm applied to the piston problem, Comput. Methods Appl. Mech. Engrg. 167 (1998) 369–391.

[5] H.H. Brenan, S.L. Campbell, L.R. Petzold, Numerical Solution of Initial-Value Problems in Differential–Algebraic Equations, North Holland, New York, 1989.

[6] H. Chen, R.L. Taylor, Vibration analysis of fluid–solid systems using a finite element displacement formulation, Int. J. Numer. Methods Engrg. 29 (1990) 683–698.

[7] A.K. Chopra, Dynamics of Structures: Theory and Applications to Earthquake Engineering, Prentice Hall, Inc., New Jersey, 1995.

[8] R.W. Clough, J. Penzien, Dynamics of Structures, McGraw-Hill, New York, 1975.

[9] R.D. Cook, D.S. Malkus, M.E. Plesha, R.J. Witt, Concepts and Applications of Finite Element Analysis, fourth ed., John Wiley and Sons, New York, 2002.

[10] B. El-Aidi, Nonlinear Earthquake Response of Concrete Gravity Dam Systems. Ph.D. Thesis, California Institute of Technology, Pasadena, 1989.

[11] C. Farhat, M. Lesoinne, N. Maman, Mixed explicit/implicit time integration of coupled aeroelastic problems: three-field formulation, geometric conservation and distributed solution, Int. J. Numer. Methods Engrg. 21 (1995) 807–835.

[12] C. Farhat, S. Piperno, B. Larrouturu, Partitioned procedures for the transient solution of coupled aeroelastic problems; Part I: model problem, theory and two-dimensional application, Comput. Methods Appl. Mech. Engrg. 124 (1995) 79–112.

[13] C. Farhat, M. Lesoinne, P. LeTallec, Load and motion transfer algorithms for fluid/structure interaction problems with non-matching discrete interfaces: momentum and energy conservation, optimal discretization and application to aeroelasticity, Comput. Methods Appl. Mech. Engrg. 157 (1998) 95–114.

[14] C.A. Felippa, A family of early-time approximations for fluid–structure interaction, J. Appl. Mech. 47 (4) (1980) 703–708.

[15] C.A. Felippa, J.A. DeRuntz, Finite element analysis of shock-induced hull cavitiation, Comput. Methods Appl. Mech. Engrg. 44 (1984) 297–337.

[16] C.A. Felippa, R. Ohayon, Mixed variational formulation of finite element analysis of acoustoelastic/slosh fluid–structure interaction, J. Fluids Struct. 4 (1990) 35–57.

[17] C.A. Felippa, K.C. Park, C. Farhat, Partitioned analysis of coupled mechanical systems, Comput. Methods Appl. Mech. Engrg. 190 (2001) 3247–3270.

[18] C.A. Felippa, Construction of customized mass–stiffness pairs using templates, ASCE J. Aerospace 19 (2006) 241–258.

[19] K.F. Graff, Wave Motion in Elastic Solids, Oxford University Press, New York, 1975.

[20] M.A. Hamdi, Y. Ousset, A displacement method for the analysis of vibrations of coupled fluid–structure systems, Int. J. Numer. Methods Engrg. 13 (1978) 139–150.

[21] T.J.R. Hughes, The Finite Element Method: Linear Static and Dynamic Finite Element Analysis, Prentice Hall, Englewood Cliffs, NJ, 1987, Reprinted by Dover, New York, 2000.

[22] L.A. Jakobsen, A finite element approach to analysis and sensitivity analysis of time dependent fluid–structure interaction systems. Ph.D. Thesis, Aalborg University, Denmark, 2002.

[23] Y. Kim, C. Yun, A spurious free four-node displacement-based fluid element for fluid–structure interaction analysis, Engrg. Struct. 19 (8) (1997) 665–678.

[24] E. Kreyszig, Advanced Engineering Mathematics, eighth ed., John Wiley and Sons, Inc., New York, 1999.

[25] J. Lighthill, Waves in Fluids, Cambridge Univ. Press, Cambridge, UK, 1978.

[26] J. Lysmer, R.L. Kuhlemeyer, Finite dynamic model for infinite media, J. Engrg. Mech. Division 95 (EM4) (1969) 859–876, Proc. ASCE.

[27] C. Michler, S.J. Hulshoff, E.H. van Brummelen, R. de Borst, A monolithic approach to fluid–structure interaction, Comput. Fluids 33 (2004) 839–848.

[28] R.D. Mindlin, H.H. Bleich, Response of an elastic cylindrical shell to a transverse step shock wave, J. Appl. Mech. 20 (1953) 180–195.

[29] C. Morand, R. Ohayon, Fluid–Structure Interaction, Wiley, Chichester, UK, 1995.

[30] R.E. Newton, Effects of cavitation on underwater shock loading – Part 1. Technical Report NPS-69-78-013, Naval Postgraduate School, Monterey, CA, 1978.

[31] R.E. Newton, Effects of cavitation on underwater shock loading – axisymmetric geometry. Technical Report NPS-69-78-017PR, Naval Postgraduate School, Monterey, CA, 1978.

[32] R.E. Newton, Finite element analysis of shock-induced cavitation. ASCE, Spring Convention, 1980, Preprint 80-110.

[33] R.E. Newton, Effects of cavitation on underwater shock loading – plane problem. Technical Report NPS-69-81-001, Naval Postgraduate School, Monterey, CA, 1981.

[34] K.C. Park, C.A. Felippa, J.A. DeRuntz, Stabilization of staggered solution procedures for fluid–structure interaction analysis, in: T. Belytschko, T.L. Geers (Eds.), Computational Methods for Fluid–Structure Interaction Problems, AMD, vol. 26, American Society of Mechanical Engineers, ASME, New York, 1977, pp. 95–124.

[35] K.C. Park, C.A. Felippa, Partitioned analysis of coupled systems, in: T. Belytschko, T.J.R. Hughes (Eds.), Computational Methods for Transient Analysis, North-Holland, Amsterdam–New York, 1983 (Chapter 3).

[36] K.C. Park, C.A. Felippa, A variational principle for the formulation of partitioned structural systems, Int. J. Numer. Methods Engrg. 47 (2000) 395–418.

[37] K.C. Park, C.A. Felippa, R. Ohayon, Partitioned formulation of internal fluid–structure interaction problems by localized Lagrange multipliers, Comput. Methods Appl. Mech. Engrg. 190 (2001) 2989–3007.

[38] K.C. Park, C.A. Felippa, G. Rebel, A simple algorithm for localized construction of nonmatching structural interfaces, Int. J. Numer. Methods Engrg. 53 (2002) 2117–2142.

[39] K.C. Park, C.A. Felippa, G. Rebel, Interfacing nonmatching finite element discretizations: the zero moment rule, in: W.A. Wall, K.-U. Bleitzinger, K. Schweizerhof (Eds.), Trends in Computational Mechanics, CIMNE, Barcelona, Spain, 2001, pp. 355–367.

[40] K.C. Park, C.A. Felippa, R. Ohayon, Reduced order modeling in coupled systems: formulations and computational algorithms, in: A. Ibrahimbegovic, B. Brank (Eds.), Engineering Structures Under Extreme Conditions, IOS Press, Amsterdam, 2006, pp. 267–289.

[41] S. Piperno, C. Farhat, Partitioned procedures for the transient solution of coupled aeroelastic problems – Part II energy transfer analysis and three-dimensional applications, Comput. Methods Appl. Mech. Engrg. 190 (2001) 3147–3170.

[42] W. Prager, Variational principles for linear elastostatics for discontinuous displacements, strains and stresses, in: B. Broger, J. Hult, F. Niordson (Eds.), Recent Progress in Applied Mechanics, The Folke–Odgvist Volume, Almqusit and Wiksell, Stockholm, 1967, pp. 463–474.

[43] Q. Qi, T.L. Geers, Evaluation of perfectly matched layers for computational acoustics, J. Comput. Phys. 139 (1997) 166–183.

[44] G. Rebel, K.C. Park, C.A. Felippa, A contact formulation based on localized Lagrange multipliers: formulation and applications to two-dimensional problems, Int. J. Numer. Methods Engrg. 54 (2002) 263–297.

[45] M.R. Ross, Coupling and simulation of acoustic fluid–structure interaction systems using localized Lagrange multipliers. Ph.D.

Thesis, University of Colorado at Boulder, 2006. <http://caswww.colorado.edu/courses/FSI.d>.

[46] M.R. Ross, M.A. Sprague, C.A. Felippa, K.C. Park, Treatment of acoustic fluid structure interaction by localized Lagrange multipliers applications, Technical Report CU-CAS-TR-02, College of Engineering, University of Colorado, Boulder, CO, 2008, Comput. Methods Appl. Mech. Engrg., to be submitted for publication.

[47] M.A. Sprague, T.L. Geers, A spectral-element method for modeling cavitation in transient fluid–structure interaction, Int. J. Numer. Methods Engrg. 60 (2004) 2467–2499.

[48] E.L. Wilson, M. Khalvati, Finite elements for the dynamic analysis of fluid–solid systems, Int. J. Numer. Methods Engrg. 19 (1983) 1657–1668.

[49] X. Yue, Development of joint elements and solution algorithms for dynamic analysis of jointed structures. Ph.D. Thesis, University of Colorado at Boulder, 2002.

[50] O.C. Zienkiewicz, D.K. Paul, E. Hinton, Cavitation in fluid–structure response (with particular reference to dams under earthquake loading), Earthquake Engrg. Struct. Dyn. 11 (1983) 463–481.